https://doi.org/10.1016/j.actamat.2020.09.031

Atomic-scale investigation of deep hydrogen trapping in NbC/α-Fe semi-coherent interfaces

Rongjian Shi [a, b], Yuan Ma [a, b], Zidong Wang [c], Lei Gao [a, b], Xu-Sheng Yang [d, e], Lijie Qiao [a, b, *], Xiaolu Pang [a, c, *]

[a] *Beijing Advanced Innovation Center for Materials Genome Engineering, University of Science and Technology Beijing, Beijing 100083, China*

[b] *Corrosion and Protection Center, University of Science and Technology Beijing, Beijing 100083, China*

[c] *School of Materials Science and Engineering, University of Science and Technology Beijing, Beijing 100083, China*

[d] *Advanced Manufacturing Technology Research Centre, Department of Industrial and Systems Engineering, The Hong Kong Polytechnic University, Hung Hom, Kowloon, Hong Kong, China*

[e] *Hong Kong Polytechnic University Shenzhen Research Institute, Shenzhen 518057, China*

* Corresponding authors.

E-mail addresses:

lqiao@ustb.edu.cn (L. Qiao), pangxl@mater.ustb.edu.cn (X. Pang).

Abstract

The precipitation of niobium carbide (NbC) is a superior approach to mitigating hydrogen embrittlement (HE). The role of the semi-coherent interface between NbC and α-Fe on hydrogen trapping and HE resistance in high-strength tempered martensitic steel was investigated in this study. High-resolution transmission electron microscopy observations are performed to

reveal the atomic-scale crystallographic orientation relationship, atomic arrangements, and associated crystalline defects in the NbC/α-Fe semi-coherent interface. We observed the Kurdjumov–Sachs orientation relationship with $(1\bar{1}\bar{1})_{NbC}$ // $(101)_{\alpha\text{-Fe}}$ and $[0\bar{1}1]_{NbC}$ // $[\bar{1}11]_{\alpha\text{-Fe}}$ between the NbC and α-Fe phases. Noticeably, two sets of misfit dislocations with Burgers vectors of $\mathbf{b}^{(1)}=a_b/2[111]$ on $(01\bar{1})$ α-Fe planes and $\mathbf{b}^{(2)}=a_b/2[1\bar{1}1]$ on (110) α-Fe planes (a_b is the lattice constant of α-Fe), which would be the deep hydrogen trapping sites, were characterized in the NbC/α-Fe semi-coherent diffuse interface. In addition, density functional theory-based first-principles calculations revealed that the deep binding energy between the NbC/α-Fe semi-coherent interface and hydrogen is 0.80 eV, which well matches the hydrogen desorption activation energy of 81.8 kJ/mol determined via thermal desorption spectroscopy experiments. These demonstrate that the nature of the deep hydrogen trapping sites of the NbC/α-Fe semi-coherent interface is the misfit dislocation core. Distinguished HE resistance was obtained and ascribed to the deep hydrogen trapping of uniformly dispersed NbC nanoprecipitates with an average diameter of 10.0 ± 3.3 nm. The strategy of deep hydrogen trapping in the NbC/α-Fe semi-coherent interface is beneficial for designing HE-resistant steels.

Keywords: Hydrogen embrittlement; Carbides; Semi-coherent interface; Steel; HRTEM.

1. Introduction

High-strength martensitic steels exhibit excellent mechanical properties, which enables them extensively applied in the automotive industry, oil and gas exploitation, and marine engineering [1-3]. Nevertheless, a critical shortcoming is the catastrophic hydrogen embrittlement (HE), which is not fully understood

for more than a century [4-6]. Recently, Chen et al. [1, 7] performed cryo-transfer atom probe tomography (APT) to directly observe abundant hydrogen at dislocations, grain boundaries, and precipitates, which can function as hydrogen traps; their work demonstrates the effectiveness of hydrogen trapping. However, for reversible traps (e.g., vacancies [8], dislocations [9]) with weak hydrogen binding energies, the captured hydrogen can escape and then accumulate along grain boundaries, thus inducing HE [10-12]. Hence, the design of deep hydrogen traps dispersed in the interior of the grains (e.g., precipitates) is urgently needed to suppress HE. Much of research has examined how face-centered cubic (fcc) carbides with rock-salt structures, especially vanadium carbide (VC) [7, 13-18], titanium carbide (TiC) [19-25], and niobium carbide (NbC) [1, 26-28], can produce substantial hydrogen traps. Furthermore, Wei et al. [29] reported that the carbides decrease in hydrogen trapping capacity in the order NbC > TiC > VC when present at the same atomic concentration. To explore the nature of deep hydrogen trapping in NbC, which, acting as high-efficiency hydrogen traps, is beneficial to develop HE-resistant steels.

Nb-microalloyed steels have been widely used due to the significant effect of NbC on precipitation hardening and the suppression of HE [30-32]. HE resistance is notably improved with the appropriate addition of Nb (~0.05 wt.%) because of the hydrogen trapping of NbC [27, 32, 33]. The activation energy of NbC precipitates is generally 40–70 kJ/mol during electrochemical and gaseous hydrogen charging [28]. Yet, for NbC, despite being extensively studied with distinguished hydrogen trapping capacity and HE resistance, no precise proposed hydrogen trapping mechanism was confirmed by atomistic investigations. A recent study suggested that deuterium atoms are trapped at the interfaces between NbC and α-Fe directly observed through APT [1]. However, various defects or imperfections in NbC/α-Fe interfaces, such as

tetrahedral or octahedral interstitial sites [24], elastic-stress fields, vacancies, and dislocations [21], are likely to trap hydrogen. Thus, there is still inexplicit comprehension of the exact location of hydrogen trapping sites in NbC/α-Fe interfaces due to the lack of APT's ability for providing structural information to correlate with its effective hydrogen detection [34].

The coherency of the precipitate/matrix interface, which is one of the most important characteristic parameters of carbides, strongly affects the hydrogen trapping ability. The hydrogen trapping sites of fully coherent precipitates are located in the elastic-stress fields around the coherent interfaces with a weak binding energy of 1.7–4.0 kJ/mol [21]. With the loss of coherency, although the incoherent carbides exhibit an extremely high binding energy (>90 kJ/mol) at carbon vacancies inside the particles, they can hardly be populated with hydrogen at room temperatures because the energy barrier is too high [19, 21, 24, 28]. Given the synergetic influence of coherency on mechanical properties and hydrogen trapping, the semi-coherent carbides, with the binding energy of 30–70 kJ/mol [13, 15, 18, 23, 24], possess more distinguished comprehensive performance. However, the nature of the hydrogen trapping sites in the semi-coherent interfaces, including misfit dislocation cores [21, 24] and surface carbon vacancies [18, 25], remains a controversial topic. The hydrogen trapping sites of disc-like semi-coherent V_4C_3 precipitates, in which the C/V atomic ratio is approximately 0.75, originate from carbon vacancies on the (001) broad surface [18]; this result was also verified by the first-principles calculations [35]. The greater difference between Fe and Nb than between Fe and V in atomic size and electronic structure [36] may account for the difference in microstructure and hydrogen trapping effectiveness between NbC and VC. Furthermore, the origin of the deep hydrogen trapping sites (~55 kJ/mol in activation energy) in semi-coherent TiC is the core of the misfit dislocation, with the technique of either thermal desorption spectroscopy (TDS) [21, 37] or first-

principles calculations [24]. Nevertheless, because of a lack of atomic-scale investigations (both experimental and computational), little evidence for misfit dislocations or other defects as the hydrogen trapping sites, particularly for the equiatomic NbC, has been reported. Hence, further validation of the nature of the hydrogen trapping sites in ellipsoidal NbC through a combination of high-resolution transmission electron microscopy (HRTEM) atomic-scale observations and first-principles calculations is urgently needed.

In the present work, we manufactured high-strength tempered martensitic steels with distinguished HE resistance ascribed to uniformly dispersed NbC nanoprecipitates. The mysterious nature of the hydrogen trapping sites in the NbC nanoprecipitate was revealed to be related to the misfit dislocations with high number density in NbC/α-Fe semi-coherent interfaces through a combination of HRTEM atomic-scale observations, first-principles calculations based on density functional theory (DFT), and TDS analysis.

2. Materials and methods

2.1 Materials

The NbC-precipitation-strengthened martensitic steel used in this study had a chemical composition of Fe-0.05C-1.10Mn-0.007P-0.002S-4.50Ni-0.53Cr-0.52Mo-0.05Nb wt.%. The steel was received as 30 mm-thick as-rolled plates. These plates were sectioned into dimensions of 30 × 30 × 70 mm^3 by electro discharge machining for further heat treatment. Samples were austenitized at 950 °C for 30 min, and followed by water quenching to obtain a full-martensitic structure; these samples are referred to as as-quenched steels (950-Q). To change the size and amount of NbC precipitates, the quenched samples were subsequently tempered at 440, 480, 520, and 560 °C for 60 min; the tempered samples are referred to as Q&T-440, Q&T-480, Q&T-520, and

Q&T-560, respectively. To preclude the influence of mechanical strength on HE susceptibility, a different quenching process (900 °C for 30 min) was also studied; the corresponding as-quenched samples are referred to as 900-Q′. A schematic of the heat-treatment process is shown in Fig. 1(A).

2.2 Microstructural observations

Quantitative X-ray diffraction (XRD) analysis was performed at ambient temperature on a TTR III X-ray diffractometer with Cu Kα radiation (wavelength, λ = 0.1542 nm). The samples were electrochemically polished in a solution of 95 vol% ethanol and 5 vol% perchloric acid at a voltage of 30 V for 15 s to relieve deformed surfaces before analysis. The diffraction patterns were recorded from 40° ≤ 2θ ≤ 120° with a step of 0.1° and count time of 15 s/step.

Samples for electron backscatter diffraction (EBSD) analysis were electropolished with 90% acetic acid and 10% perchloric acid. The EBSD analysis and fracture surface observation of the samples after mechanical testing were carried out by field-emission scanning electron microscope (SEM, Zeiss Supra^{TM} 55) operated at 20 kV.

The microstructure, distribution, and energy-dispersive X-ray spectroscopy (EDS) of NbC nanoprecipitates in the investigated steels were observed by transmission electron microscopy (TEM, JEOL JEM-2100F) operated at 200 kV. The pre-thinned TEM foils with a thickness of 30–50 μm were further thinned in a 10 vol.% $HClO_4$ methanol electrolyte by twin-jet electropolishing at −30 °C. The distribution of precipitates was characterized by TEM using carbon extraction replicas with a copper (Cu) microgrid; a detailed experimental procedure is reported elsewhere [2]. The HRTEM images were Fourier filtered via fast Fourier transformation (FFT) to enhance the visualization for better contrast without affecting the facticity [38].

2.3 TDS analysis

TDS analysis was undertaken to identify the hydrogen trapping capacity. The specimens 25 mm in length and 5 mm in diameter were electrochemically hydrogen charged in 0.05 mol/L H_2SO_4 + 0.22 g/L thiourea with a current density of 5 mA/cm^2 for 10 h. All pre-charged specimens were subsequently cleaned with distilled water and ethanol and air dried (within 5 min) before TDS analysis. The TDS experiments were performed with quadrupole mass spectroscopy at a certain heating rate (100, 200, or 300 °C/h in this study), immediately after the vacuum level was sufficiently low (~10^{-11} Pa).

2.4 Mechanical testing

Slow strain rate tensile (SSRT) tests were conducted at room temperature to evaluate the HE susceptibility. Specimens with cylindrical gauge dimensions of 5 mm diameter and 25 mm length were polished using SiC papers to 2000 grit progressively and then cleaned ultrasonically in acetone. Uniaxial SSRT tests of the hydrogen uncharged and pre-charged samples were performed on an MTS 647 tensile machine at constant strain rate of 10^{-5} s^{-1}, which corresponds to a crosshead speed of 0.00025 mm/s, with a load cell of 35 kN. Hydrogen was electrochemically pre-charged in deionized water containing 0.05 mol/L H_2SO_4 + 0.22 g/L thiourea. The cathode was connected to the specimen, and the anode was connected to a platinum wire; the current density was 1 or 5 mA/cm^2, and the current was applied for 10 h at room temperature. After pre-charging, the samples were immediately electroplated with cadmium (Cd, ~20 μm thick) to prevent hydrogen from escaping before the SSRT tests. In addition, the hydrogen concentration was measured by Bruker G4 PHOENIX DH hot-extraction analyser at 800 °C for 20 min after hydrogen charging for each tensile specimen.

2.5 DFT calculations

The different equilibrium NbC/α-Fe interfaces, including coherent and semi-coherent ones, and the binding energies between hydrogen and a particular interface were investigated by first-principles calculations based on DFT [39, 40] in the Vienna Ab-initio Simulation Package (VASP) [41, 42]. While the projector-augmented wave (PAW) [43] method described the core electrons, the electron exchange and correlation were modeled with Perdew–Burke–Ernzerhof (PBE) method [44]. A plane wave cut-off energy of 400 eV was selected. All calculations were carried out as spin-polarized. For structural relaxation, all atoms were fully relaxed with the residual force on each atom less than 0.02 eV/Å. The total energy was converged to 10^{-6} eV for the calculations. The Brillouin zone for the NbC/α-Fe interface structure was sampled employing Monkhorst–Pack grids with a 3 × 3 × 1 *k*-point mesh. The optimized DFT lattice parameters are $a = b = c = 4.48$ Å for NbC and $a = b = c = 2.83$ Å for α-Fe, which are consistent with the experimental values of $a = b = c = 4.47$ Å [45] for NbC and $a = b = c = 2.86$ Å [46] for α-Fe in this study, respectively.

3. Results and discussion

3.1 Microstructural characterization

The XRD profiles in Fig. 1(B) indicate that the investigated steels are comprised entirely of body-centered cubic (bcc) α-martensite single phase, with the amount of retained austenite below the detection limit (see Fig. S1 in Supplementary Information). Fig. 2 shows representative microstructural characterization results for the investigated Q&T-480. The EBSD image in Fig. 2(A) presents the microstructure of the equiaxed grains with an average grain diameter of 5.3 ± 1.7 μm, as indicated in the inset. Fig. 2(B) is a typical TEM

image showing the distribution of martensite laths (yellow broken lines) and nanoprecipitates (arrows). The bright-field and the corresponding dark-field images taken from the dotted circles in the selected-area diffraction pattern in the inset are presented in Fig. 2(C–D), respectively. The nanoprecipitates (arrows) are distributed uniformly inside the grain. An enlarged view of the distribution of nanoprecipitates is shown in Fig. 2(E). Fig. 2(F) is the corresponding EDS result of the dashed circle in Fig. 2(E), indicating the nanoprecipitates are NbC. The average NbC nanoprecipitate diameters are 10.0 ± 3.3 nm, as shown in Fig. 2(G).

3.2 Atomic-scale characterization of NbC/α-Fe semi-coherent interface

Fig. 3 gives the detailed atomic-scale characterization of the NbC/α-Fe interface in Q&T-480, as revealed by HRTEM observation projected along the $[0\bar{1}1]_{NbC}$ // $[\bar{1}11]_{\alpha\text{-}Fe}$ directions. Fig. 3(A) presents the HRTEM image of a typical NbC nanoprecipitate surrounded by the α-Fe matrix, and the inset shows the corresponding two sets of FFT spots. Fig. 3(B1–B2) and Fig. 3(B3–B4) are the FFT patterns and inversed FFT (IFFT) images taken from the selected red and blue dashed boxes in Fig. 3(A), respectively, showing the atomic structures of the bcc α-Fe matrix and fcc NbC nanoprecipitate phases, projected along the $[0\bar{1}1]_{NbC}$ // $[\bar{1}11]_{\alpha\text{-}Fe}$ zone axis. On the basis of the FFT patterns and Fourier-filtered HRTEM images, the atomic spacing of some typical crystallographic planes can be measured directly to verify the existence of these two phases, e.g., $d_{(\bar{1}\bar{1}0)\alpha\text{-}Fe}$ = 2.03 Å and $d_{(\bar{1}\bar{1}\bar{1})NbC}$ = 2.61 Å. Accordingly, the diffraction spots from Fig. 3(B1) and (B3) are schematically summarized in Fig. 3(C), indicating that the orientation relationship (OR) between the NbC and α-Fe is typical semi-coherent Kurdjumov–Sachs (K–S) OR [47-49] with $(1\bar{1}\bar{1})_{NbC}$ // $(101)_{\alpha\text{-}Fe}$ and $[0\bar{1}1]_{NbC}$ // $[\bar{1}11]_{\alpha\text{-}Fe}$. Fig. 3(D) gives the Fourier-

filtered HRTEM image on the NbC/α-Fe interfacial structure with the K–S OR. We premise that all dislocation lines are parallel to the electron beam direction of $[0\bar{1}1]_{NbC}$ // $[\bar{1}11]_{\alpha\text{-Fe}}$ [50, 51]. A high density of misfit dislocations, which are indicated by the "⊥" symbols and the Burgers circuits (dashed-line circuit), are observed for the NbC/α-Fe semi-coherent interface, as shown in Fig. 3(D). Fig. 3(E) is an enlarged image corresponding to the dotted region in Fig. 3(D). The interface between $(1\bar{1}\bar{1})_{NbC}$ and $(101)_{\alpha\text{-Fe}}$ with the K–S OR is diffuse and semi-coherent. Two sets of misfit dislocations with Burgers vectors of $\mathbf{b}^{(1)} = a_b/2[111]$ on $(01\bar{1})$ α-Fe planes and $\mathbf{b}^{(2)} = a_b/2[1\bar{1}1]$ on (110) α-Fe planes are observed inside the NbC/α-Fe semi-coherent interfacial zone, where a_b is the lattice constant of α-Fe. These dislocations are mixed dislocations with components $\mathbf{b}_{[12\bar{1}]}$, $\mathbf{b}_{[101]}$, and $\mathbf{b}_{[\bar{1}11]}$. $\mathbf{b}_{[12\bar{1}]}$ and $\mathbf{b}_{[101]}$ are the edge dislocation components, and vector $\mathbf{b}_{[\bar{1}11]}$ is perpendicular to the image planes, which is the screw dislocation component. The lattice misfit strain, *f*, between $[211]_{NbC}$ and $[12\bar{1}]_{\alpha\text{-Fe}}$ is f = 16.61% (Fig. S2 in Supplementary Information). These two Burgers vectors have the same component of $b_{[12\bar{1}]} = b^{(1)}_{[12\bar{1}]} = b^{(2)}_{[12\bar{1}]} = 1.17$ Å along the $[12\bar{1}]_{\alpha\text{-Fe}}$ direction. To substantially release the lattice misfit strain of 16.61%, the spacing of the misfit dislocation array, $L_{[12\bar{1}]}$, is calculated by the following equation [51]:

$$L_{[12\bar{1}]} = b_{[12\bar{1}]}/f \quad (1)$$

$L_{[12\bar{1}]}$ should be 7.0 Å, which is almost equivalent to the average length of 6 $(12\bar{1})$ α-Fe planes. In addition, these Burgers vectors have the components of $b^{(1)}_{[101]} = -b^{(2)}_{[101]} = 2.03$ Å along the $[101]_{\alpha\text{-Fe}}$ and $b^{(1)}_{[\bar{1}11]} = -b^{(2)}_{[\bar{1}11]} = 0.83$ Å along the $[\bar{1}11]_{\alpha\text{-Fe}}$. Moreover, the number ratio for the two sets of observed

dislocations is approximately 1:1, as indicated in Fig. 3(D–E). This ratio can significantly reduce the long-range stress field between the NbC/α-Fe interface without rotation because the $\mathbf{b}^{(1)}$ and $\mathbf{b}^{(2)}$ misfit dislocations have the same value but the opposite directions for their Burgers vector components along the [101] and $[\bar{1}11]$ α-Fe directions [24, 51]. In addition, two sets of misfit dislocations with Burgers vectors of $-\mathbf{b}^{(1)}$ and $-\mathbf{b}^{(2)}$ are distributed in the left side of the particle in Fig. 3(D) and should be the other side of the $\mathbf{b}^{(1)}$ and $\mathbf{b}^{(2)}$ misfit dislocation loops [52], respectively. Because of the same diffuse interfacial structure with $(1\bar{1}\bar{1})_{NbC}$ // $(101)_{\alpha\text{-Fe}}$, these two sets of $-\mathbf{b}^{(1)}$ and $-\mathbf{b}^{(2)}$ misfit dislocations are also distributed on every 6 $(12\bar{1})$ α-Fe planes.

Furthermore, approximately 6 $\mathbf{b}^{(1)}$ and 6 $\mathbf{b}^{(2)}$ misfit dislocations are observed in Fig. 3(D). The amount of misfit dislocations, N, could be obtained by the following equation:

$$N = d_{[12\bar{1}]} / L_{[12\bar{1}]} \tag{2}$$

where $d_{[12\bar{1}]}$ is the distance along the $[12\bar{1}]_{\alpha\text{-Fe}}$ direction of a NbC nanoprecipitate, and $L_{[12\bar{1}]} = 7.0$ Å. In Fig. 3(D), the distance along the $[12\bar{1}]_{\alpha\text{-Fe}}$ direction of the NbC particle is 8.5 nm, and $N = 8.5\ \text{nm} / 7.0\ \text{Å} \approx 12$, which is coincident with the number of observed misfit dislocations. In addition, the HRTEM image of a smaller NbC with the surrounding α-Fe projected along $[0\bar{1}1]_{NbC}$ // $[\bar{1}11]_{\alpha\text{-Fe}}$ is shown in Fig. 4(A), and the corresponding FFT patterns is indicated in the inset. The interfacial structure for the NbC/α-Fe semi-coherent interface comprises two sets of misfit dislocations with 4 $\mathbf{b}^{(1)}$ and 4 $\mathbf{b}^{(2)}$, as indicated in Fig. 4(B). The distance along the $[12\bar{1}]_{\alpha\text{-Fe}}$ direction of this smaller NbC particle is approximately 5.5 nm, and $N = 5.5\ \text{nm} / 7.0\ \text{Å} \approx 8$, which is also coincident with the observed misfit dislocations. Hence, the amount of misfit dislocations in NbC/α-Fe semi-coherent interface along the

$[0\bar{1}1]_{NbC}$ // $[\bar{1}11]_{\alpha\text{-Fe}}$ directions can be obtained by $N = d_{[12\bar{1}]}/7.0$ Å. In addition, Fig. 4(C–D) shows schematic of the lattice correspondence for the NbC (blue) and α-Fe (red). The defined crystallographic coordinate system for fcc NbC and bcc α-Fe structures is indicated in Fig. 4(C). In Fig. 4(D), when $[\bar{1}11]_{\alpha\text{-Fe}}$ rotated to $[001]_{\alpha\text{-Fe}}$, the $[0\bar{1}1]_{NbC}$ could not rotate to $[1\bar{1}0]_{NbC}$ (with inclined angle at least 5°) correspondingly so that the K–S OR in this study is neither the traditional Baker–Nutting (B–N) OR [53], with $(001)_{carbide}$ // $(010)_{\alpha\text{-Fe}}$ and $[1\bar{1}0]_{carbide}$ // $[001]_{\alpha\text{-Fe}}$, nor the Nishiyama–Wassermann (N–W) OR [48], with $(111)_{carbide}$ // $(110)_{\alpha\text{-Fe}}$ and $[1\bar{1}0]_{carbide}$ // $[001]_{\alpha\text{-Fe}}$.

In the present study, we first observed two sets of misfit dislocations with Burgers vectors of $\mathbf{b}^{(1)} = a_b/2\,[111]$ on $(01\bar{1})$ α-Fe planes and $\mathbf{b}^{(2)} = a_b/2\,[1\bar{1}1]$ on (110) α-Fe planes along the $[0\bar{1}1]_{NbC}$ // $[\bar{1}11]_{\alpha\text{-Fe}}$ directions in the NbC/α-Fe semi-coherent interface with the K–S OR. Misfit dislocations were barely observed at the carbide/α-Fe (001) broad interfaces with the B–N OR [18, 21, 54]; thus, the carbon vacancies on the (001) platelets were speculated to be the nature of the hydrogen trapping sites of V_4C_3 precipitates [17, 18]. In addition, a recent study [1] provided direct observation of deuterium atoms trapped at the interfaces between NbC and α-Fe. However, for the carbides that lack sufficient carbon vacancies, such as NbC or even TiC, the nature of the hydrogen trapping sites is a long-term controversial scientific issue. Therefore, the misfit dislocations with high number density at the NbC/α-Fe semi-coherent interface in this study could be effective deep trapping sites and therefore require further investigation. The DFT calculations and TDS experiments are presented in the following sections to demonstrate the deep hydrogen trapping in the NbC/α-Fe semi-coherent interface.

3.3 Investigation of deep hydrogen trapping in the NbC/α-Fe semi-coherent interface via DFT calculations

In this section, we simulated three typical interfaces: the (001) NbC/α-Fe coherent interface with the B–N OR, the (001) NbC/α-Fe coherent interface with surface carbon vacancies, and the NbC/α-Fe semi-coherent interface with the K–S OR based on this study. The DFT calculations were performed to evaluate the interactions between hydrogen and different interfaces and the associated energetics. Fig. 5 shows the representative atomic structures used in the DFT calculations of different NbC/α-Fe interfaces, with the details of relaxed hydrogen atoms shown in the enlarged insets. The binding energy between hydrogen atoms and the NbC/α-Fe interface, E_b, is defined as [46, 55, 56]

$$E_b = E_0^{tot} + E_H^{iso} - E_H^{tot} \quad (3)$$

where E_0^{tot}, E_H^{iso}, and E_H^{tot} are the total energy before segregation of hydrogen, the energy of an isolated hydrogen atom, and the total energy of the supercell with one interstitial hydrogen, respectively. Notably, a positive binding energy represents a favorable attraction between hydrogen and defects. The characteristic binding energies from our DFT calculations (Calc) and references (Refs.) are summarized in Table 1.

The (001) NbC/α-Fe coherent interface with the B–N OR before and after hydrogen segregation are shown in Fig. 5(A–B), respectively. The calculated E_b between hydrogen and NbC/α-Fe coherent interface is 0.19 eV, which is approximately the same as the segregation energy at the TiC/α-Fe coherent interface because of the elastic expansion of the α-Fe [21, 24]. The relaxed hydrogen atom is located in the α-Fe lattice in the vicinity of the interface, as indicated in the enlarged inset of Fig. 5(B). In addition, the $(020)_{\alpha\text{-Fe}}$ planar spacings in Fig. 5(A) of the first and third α-Fe layer close to the interface are 1.50 Å and 1.47 Å, respectively. Therefore, the elastic strain field of the α-Fe

crystal due to the carbide/α-Fe lattice mismatch is the primary hydrogen trapping site in the coherent interface. Fig. 5(C–D) presents the (001) NbC/α-Fe coherent interface with a single surface carbon vacancy before and after hydrogen segregation, respectively. The obtained E_b between hydrogen and the surface carbon vacancy at the NbC/α-Fe coherent interface is 0.33 eV, which is more favorable for hydrogen trapping than the perfect coherent interface. The center of the carbon vacancy in the dashed circle of Fig. 5(D) is favorable for hydrogen occupation, consistent with a previous report [24]. Given the simulation of the NbC/α-Fe semi-coherent interface with the $(1\bar{1}\bar{1})_{NbC}$ // $(101)_{\alpha\text{-Fe}}$ and $[0\bar{1}1]_{NbC}$ // $[\bar{1}11]_{\alpha\text{-Fe}}$ K–S OR based on the present study in section 3.2, Fig. 5(E–F) shows the NbC/α-Fe semi-coherent interface with the K–S OR before and after hydrogen segregation, respectively. The E_b between hydrogen and the semi-coherent interface is 0.80 eV, which is much stronger than the E_b in the case of TiC (0.50 eV) [24]. The configuration in which the Fe atoms have two Nb and two C as nearest atoms is related to the misfit dislocation cores, which substantially consists of an extra Fe atomic plane [24]. In Fig. 5(E), the supercell comprises three columns of Nb atoms or four columns of Fe atoms along the $[211]_{NbC}$ // $[12\bar{1}]_{\alpha\text{-Fe}}$ directions so that the simulated NbC/α-Fe semi-coherent interface consists of a misfit dislocation. The relaxed hydrogen atom is located in the vicinity of the semi-coherent interface between α-Fe and NbC, most likely ascribed to the presence of the misfit dislocation core, as indicated in Fig. 5(F). This is consistent with the atomistic simulation that hydrogen mainly aggregates at the dislocation cores [55].

Thus, from the above analysis, compared with the aforementioned interfaces (e.g., coherent interfaces with or without surface carbon vacancies) in our DFT calculations and those in the references, the NbC/α-Fe semi-coherent interface with the K–S OR exhibits a stronger binding energy, which means deeper hydrogen trapping. The misfit dislocation cores are particularly

probable hydrogen trapping sites in the NbC/α-Fe semi-coherent interface based on the energy point of view.

3.4 Determination of the deep hydrogen trapping of NbC

To examine the hydrogen trapping capacity of the NbC-strengthened steel, the hydrogen desorption activation energy, E_a, of the pre-charged Q&T-480 was analyzed under three different heating rates (100, 200, and 300 °C/h), as indicated in Fig. 6(A). The E_a is obtained by the following Kissinger's first-order reaction-kinetic formula [59, 60]:

$$\frac{\partial \ln\left(\phi/T_p^2\right)}{\partial\left(1/T_p\right)} = -\frac{E_a}{R} \tag{4}$$

where ϕ, T_p, and R are the heating rate, desorption peak temperature, and gas constant, respectively. Fig. 6(B) presents the relation between $\ln(\phi/T_p^2)$ and $1/T_p$ in the Q&T-480, and the E_a was estimated from the line slope for each peak. The values of the E_a corresponding to Peak 1 and Peak 2 are 19.7 ± 2.4 kJ/mol and 81.8 ± 10.5 kJ/mol, respectively. The E_{a1} = 19.7 kJ/mol of Peak 1 is in agreement with the values reported in numerous other studies [23, 56, 61, 62], which confirms that Peak 1 is induced by the dislocations and lath boundaries as reversible hydrogen traps. Peak 2, in particular, is generated by the desorption of hydrogen from the irreversible traps with high activation energy (E_{a2} = 81.8 kJ/mol).

Using a combination of HRTEM atomic-scale observations, first-principles calculations, and TDS analysis, we investigated the correlation between NbC/α-Fe semi-coherent interfaces and deep hydrogen trapping in NbC-precipitation-strengthened martensitic steels. The binding energy between hydrogen and the NbC/α-Fe semi-coherent interface, as calculated by DFT, is 77.2 kJ/mol (0.80 eV), which is slightly weaker than the hydrogen desorption activation energy of Peak 2 in Q&T-480, E_{a2} = 81.8 kJ/mol, obtained by TDS. However, the E_b and

the corresponding E_a exhibit the following relationship in this study [20, 35, 60]:

$$E_a = E_b + E_d^{\alpha\text{-Fe}} \quad (5)$$

where $E_d^{\alpha\text{-Fe}}$ is the energy barrier for hydrogen diffusion in α-Fe, which is also the saddle-point energy for the NbC/α-Fe semi-coherent interface [24]. The $E_d^{\alpha\text{-Fe}}$ is considered to be 6.9–8.7 kJ/mol [21, 35]. Hence, the modified activation energy calculated by DFT is approximately 85.0 kJ/mol, which well matches the E_{a2} = 81.8 kJ/mol obtained from TDS. Hence, Peak 2 in the TDS reveals the deep hydrogen trapping of NbC nanoprecipitates in Q&T-480 with E_{a2} = 81.8 kJ/mol. This result also validates the DFT results revealing that the deep hydrogen trapping sites in the NbC/α-Fe semi-coherent interface are the misfit dislocation cores.

Furthermore, the density of the hydrogen traps, which is less understood, is of great importance to improve HE resistance. A generalized equation to estimate the density of possible hydrogen traps in sphere-shaped carbides, N_t, which assumes that the trapping sites are arranged periodically at the carbide/matrix interface, is given by [56]

$$N_t = \frac{13r^2}{l^3 p^2 N_A} \quad (6)$$

where r, l, p, and N_A are the radius of carbides, the mean distance between adjacent carbides, the periodicity of trapping sites, and the Avogadro number, respectively. For the misfit dislocations at NbC/α-Fe semi-coherent interface in the present work, r = 5 nm, l = 45 ± 15 nm, and the periodicity, p, is equivalent to the spacing of the adjacent misfit dislocation array, $L_{[12\bar{1}]}$ = 0.7 nm, which is obtained from section 3.2. According to these analyses, the hydrogen trap density for NbC in the present work is ~10^{-8} mol/mm^3, which is consistent with the results (10^{-10}–10^{-7} mol/mm^3) in Refs. [56, 58]. This relatively high density of the deep hydrogen traps in NbC/α-Fe interface might have an important role in HE resistance, which is presented in the following section.

3.5 Effect of deep hydrogen trapping of NbC on the HE resistance

To further investigate the influence of deep hydrogen trapping of NbC on the HE resistance, the HE susceptibility of 950-Q, 900-Q′, Q&T-440, Q&T-480, Q&T-520, and Q&T-560 steels was evaluated using SSRT tests. Fig. 7 presents the dependence of the engineering stress–strain curves on various heat-treatment conditions and the hydrogen pre-charging current density (1 mA/cm^2 and 5 mA/cm^2 for 10 h). In general, the HE susceptibility was strongly related to the quenching temperature, tempering temperature, and hydrogen charging current density. The HE index, I_{HE}, which indicates the degree of the ductility loss by hydrogen pre-charging, could be obtained by the following equation [63]:

$$I_{HE}(\%) = \frac{\delta_0 - \delta_H}{\delta_0} \times 100 \quad (7)$$

where δ_0 and δ_H are the elongations of SSRT tests without and with hydrogen pre-charging, respectively. The evaluated mechanical properties, including the I_{HE} values as well as the measured hydrogen concentrations, are summarized in Table 2. The relationship between HE susceptibility, I_{HE}, and hydrogen content is shown in Supplementary Fig. S3. The hydrogen pre-charged specimens expressed a lower ductility compared with the uncharged ones, and HE became more sensitive with increasing hydrogen-charging current density, especially at 5 mA/cm^2. The HE susceptibility was most severe for 950-Q at 5 mA/cm^2, with 89.4%, which is coincident with that the HE susceptibility increases dramatically with improving mechanical strength [64, 65]. However, after a tempering treatment, the HE resistance was improved greatly, particularly at 480 °C tempering (Q&T-480), where the HE susceptibility was 5.1% and 13.8% at pre-charging current densities of 1 mA/cm^2 and 5 mA/cm^2, respectively. Although the tensile strength decreased when the tempering temperature was greater than 480 °C, HE susceptibility again increased.

To further investigate the HE susceptibility, we used SEM to observe the

fractured surfaces after SSRT tests. All of the specimens exhibited ductile fracture surfaces with micro-void coalescence (MVC) dimples when tested in air, as shown in Supplementary Fig. S4. Fig. 8 illustrates the SEM fracture surfaces after SSRT tests of 950-Q, 900-Q′, Q&T-480, and Q&T-560 in which the specimens were pre-charged at 5 mA/cm^2 for 10 h. Four zones are identified: (I) a typical brittle crack initiation region (B), (II) a typical ductile crack initiation zone (D), (III) a crack propagation region (P), and (IV) a shear lip region (S). Indications of brittle regions with no necking were observed in the 950-Q steel, in which the B region exhibited brittle fractures of a mixture of intergranular and quasi-cleavage features, as illustrated in Fig. 8(A–B). The intergranular fracture was confirmed by the faceted fracture and numerous intergranular cracks (indicated by arrowheads in Fig. 8B) [66]. Fig. 8(C) and (G) indicate that cracks in 900-Q′ and Q&T-560 initiated from transgranular quasi-cleavage fracture, as shown in Fig. 8(D) and (H), respectively. The periphery of the dotted line in Fig. 8(D) and (H) is the Cd electroplated layer, as indicated by “Cd”. However, for the Q&T-480 specimen, no brittle region is observed in Fig. 8(E–F). The periphery comprised of shallow MVC dimples, which can be considered mixed shear and cup-cone fracture, as illustrated by arrows in Fig. 8(F). These results, combined with the engineering stress–strain curves from SSRT tests and the observations of fracture surfaces, indicate that the Q&T-480 steel exhibited the most distinguished HE resistance.

HE susceptibility can be discussed on the basis of different hierarchies of microstructures, including the dislocations, lath boundaries, grain boundaries, and NbC in the present study. Representative SEM and TEM images of the investigated steels are presented in Supplementary Figs. S5–S6, respectively. All of the specimens are composed entirely of martensite laths, with lath widths of 200–400 nm. The substructure of all of the samples consisted of tangled dislocations with high density. For the as-quenched 950-Q, the hydrogen-

induced brittle fractures (Fig. 8A–B) is initiated by the attendant hydrogen accumulated at the grain boundaries with the E_b of 40–50 kJ/mol [11, 12, 67], which is the synergistic reaction of the hydrogen enhanced localized plasticity (HELP) [68] and the hydrogen-enhanced decohesion (HEDE) mechanisms [10, 69].

The lath boundary is a low-angle grain boundary comprised of edge and screw dislocations [69]. Dislocations are important to HE, and the cores and elastic fields of dislocations are the main hydrogen trapping sites [61]. The analyses of the dislocation densities for the 900-Q′, Q&T-480, and Q&T-560 steels by XRD are indicated in Fig. 9. The full-width at half-maximum (FWHM) was measured among (110), (200), (211), (220), and (310) planes, as shown in Fig. 9(A–E), respectively. The Williamson–Hall (WH) method is used for determining dislocation density [70]. The WH equation is obtained by the following [71]:

$$\delta_{hkl}\cos\theta_{hkl}/\lambda = 1/D + 4e\sin\theta_{hkl}/\lambda \quad (8)$$

where θ_{hkl}, λ, D, and e are the diffraction angle at the peak, X-ray wavelength, the average size of the coherently diffracting domains, and effective mean microstrain, respectively; δ_{hkl} is the FWHM of the diffraction peak at θ_{hkl}. Fig. 9(F) presents the relation between $\delta_{hkl}\cos\theta_{hkl}/\lambda$ and $4\sin\theta_{hkl}/\lambda$; the value of e was estimated from the line slope for each sample. The dislocation density, ρ, is obtained by the following equation [70]:

$$\rho = 14.4\, e^2/b^2 \quad (9)$$

where b is the value of Burgers vector. The dislocation densities for 900-Q′, Q&T-480, and Q&T-560 were calculated to be $(3.9 \pm 0.2) \times 10^{14}$ m^{-2}, $(2.8 \pm 0.1) \times 10^{14}$ m^{-2}, and $(2.1 \pm 0.1) \times 10^{14}$ m^{-2}, respectively. After quenching and tempering, the dislocation density decreased monotonically with increasing tempering temperature. The 900-Q′ could trap an abundance of hydrogen because of its high dislocation density. However, hydrogen trapped by the

dislocations can escape from the trapping sites during plastic deformation because of its weak binding energy and then accumulate in local regions [72-74], thus inducing quasi-cleavage fracture (Fig. 8C–D).

NbC nanoprecipitates can trap hydrogen irreversibly to enhance HE resistance [1, 26, 27]. Fig. 10(A–D) show representative TEM micrographs of nanoprecipitates uniformly distributed in tempered steels by carbon extraction replicas. We conducted EDS analysis to analyze the composition and crystal structures of the nanoprecipitates (Fig. 10A–D). The EDS results shown in the insets indicate that these nanoprecipitates all include Nb. The HRTEM image of one nanoparticle in the Q&T-480, viewed along the $[011]_{NbC}$ direction, is presented in the inset of Fig. 10(B). The fcc rock-salt structure and the atomic planar spacings of $d_{(11\bar{1})}$ = 2.60 Å, $d_{(1\bar{1}1)}$ = 2.60 Å, and $d_{(200)}$ = 2.23 Å measured from the lattice planes correspond to the $(11\bar{1})$, $(1\bar{1}1)$, and (200) crystallographic planes of NbC, respectively. The nanoprecipitates were fully dissolved during the austenitization; thus, no precipitate was observed in the as-quenched samples (950-Q and 900-Q′). The size and amount of nanoprecipitates differ substantially among the tempered steels. The carbide size distribution is indicated in Fig. 10(E), where the distribution within a diameter of 30 nm is shown in the enlarged inset. The average nanoprecipitate diameters for Q&T-440, Q&T-480, Q&T-520, and Q&T-560 are 7.4 ± 2.6 nm, 10.0 ± 3.3 nm, 12.5 ± 8.2 nm, and 17.8 ± 10.7 nm, respectively. When the tempering temperature was increased from 440 to 560 °C, the average diameter of the nanoprecipitates tended to grow monotonically, with the number density tempestuously decreasing, especially at temperatures higher than 480 °C.

The TDS analysis was conducted from ambient temperature to 600 °C at a heating rate of 100 °C/h to examine the hydrogen trapping capacity of 900-Q′, Q&T-480, and Q&T-560, as shown in Fig. 11, where the TDS profiles in the

range 300–500 °C are indicated in the enlarged inset. For the as-quenched 900-Q′ steel, a single broad peak at around 130 °C corresponds to the reversible traps, which are assumed to be martensitic lath boundaries, low-angle grain boundaries, vacancies, and high density of dislocations with activation energies from 15 to 35 kJ/mol [75, 76]. The hydrogen desorption curves of Q&T-480 and Q&T-560 exhibit two distinct peaks, with the first peak (Peak 1) at 130 °C and the second peak (Peak 2) at approximately 350 °C. The NbC nanoprecipitates were attributed to the irreversible hydrogen traps in Peak 2 (Fig. 6). The Q&T-480 shows a much higher Peak 2 than Q&T-560, which indicates that the Q&T-480 contains many more deep hydrogen traps on account of its more abundant NbC nanoprecipitates; the Q&T-480 consequently exhibits distinguished HE resistance. However, the Q&T-560, with very few coarsened NbC nanoprecipitates, was unable to trap hydrogen effectively, leading to brittle quasi-cleavage fracture (Fig. 8G–H).

3.6 Nature of the deep hydrogen trapping sites in NbC/α-Fe semi-coherent interface

Fig. 12 shows a comparison of the hydrogen trapping ability and HE resistance of the samples prepared in this work and those reported in previous studies. A map of the hydrogen activation energy versus different hydrogen traps reveals the deep hydrogen trapping of the NbC/α-Fe semi-coherent interface in this work, as compared with dislocations, grain boundaries, coherent interfaces, and semi-coherent interfaces of nanoprecipitates that served as hydrogen traps in previous studies (Fig. 12A). The map of HE susceptibility versus ultimate tensile strength of high-strength steels in previous studies and this work (Q&T-440 and Q&T-480 are indicated) reveals the distinguished HE resistance as well as high strength ascribed to the deep hydrogen trapping of NbC in this work, as indicated Fig. 12(B). The data

activation energy and HE susceptibility data in these reported studies were acquired from Supplementary Table S1 and Table S2.

Fig. 13(A–C) illustrate schematically three different HE and hydrogen trapping models. For the as-quenched high-strength steels without NbC nanoprecipitates (e.g., 950-Q steel in this study), hydrogen accumulates at the grain boundaries under high stress, ultimately inducing intergranular fracture with extremely high HE susceptibility, as shown in Fig. 13(A). However, the tempered steels with the uniformly dispersed high-density NbC nanoprecipitates (e.g., Q&T-480) could trap hydrogen irreversibly, resulting in high HE resistance, as indicated in Fig. 13(B). Fig. 13(C) presents the transgranular quasi-cleavage fracture with relatively high HE susceptibility initiated from the steels (e.g., Q&T-560) containing few coarsened NbC nanoprecipitates with the weak hydrogen trapping capacity. A schematic of the hydrogen trapping in NbC/α-Fe semi-coherent interface with misfit dislocations is summarized in Fig. 13(D). The insets show the atomic structures of interior NbC, α-Fe, and the NbC/α-Fe interface. The schematic energy profile across the misfit dislocations at the NbC/α-Fe semi-coherent interface, indicated by the white line, elucidates the deep hydrogen trapping of the misfit dislocations. According to the previously discussed DFT calculations and TDS experiments, the misfit dislocation cores are the most effective deep hydrogen trapping sites in the NbC/α-Fe semi-coherent interface.

4. Conclusions

In summary, we have investigated the nature of the deep hydrogen trapping in NbC/α-Fe semi-coherent interfaces via HRTEM atomic-scale observations, first-principles calculations, and TDS analyses. The distinguished HE resistance was obtained because of the deep hydrogen trapping of the uniformly dispersed NbC nanoprecipitates, as revealed through a combination

of systematic SSRT mechanical tests with and without pre-charged hydrogen and SEM observations of fracture surfaces. The main conclusions are summarized as follows.

(1) HRTEM atomic-scale observations reveal K–S OR at the NbC/α-Fe semi-coherent interfaces, with $(1\bar{1}\bar{1})_{NbC}$ // $(101)_{\alpha\text{-Fe}}$ and $[0\bar{1}1]_{NbC}$ // $[\bar{1}11]_{\alpha\text{-Fe}}$. Two sets of misfit dislocations with high number density and with Burgers vectors of $\mathbf{b}^{(1)} = a_b/2\,[111]$ on $(01\bar{1})$ α-Fe planes and $\mathbf{b}^{(2)} = a_b/2\,[1\bar{1}1]$ on (110) α-Fe planes are observed inside the NbC/α-Fe semi-coherent interfacial zone. The number ratio for the two sets of dislocations is approximately 1:1, and the amount of misfit dislocations along the $[0\bar{1}1]_{NbC}$ // $[\bar{1}11]_{\alpha\text{-Fe}}$ directions is obtained by $d_{[12\bar{1}]}$/7.0 Å, where $d_{[12\bar{1}]}$ is the distance along the $[12\bar{1}]_{\alpha\text{-Fe}}$ direction of NbC nanoprecipitates.

(2) First-principles calculations based on DFT revealed that the binding energy between hydrogen and the NbC/α-Fe semi-coherent interface with the K–S OR is 0.80 eV, which well matches the hydrogen desorption activation energy of 81.8 kJ/mol obtained by TDS analysis. The NbC/α-Fe semi-coherent interface with the K–S OR is more favorable for hydrogen occupation than the B–N OR coherent interface with or without surface carbon vacancies. The misfit dislocation cores are the most effective hydrogen trapping sites in the NbC/α-Fe semi-coherent interface.

(3) The best obtained HE resistance was ascribed to the deep hydrogen trapping of the uniformly dispersed high-density NbC nanoprecipitates with an average diameter of 10.0 ± 3.3 nm when tempered at 480 °C for 60 min. The HE susceptibility was 13.8% for Q&T-480 pre-charged at 5 mA/cm^2 for 10 h.

(4) This strategy of deep hydrogen trapping in NbC/α-Fe semi-coherent interface and the distinguished HE resistance is beneficial in the design of HE-resistant steels.

Acknowledgments

The authors acknowledge the financial support received from the National Natural Science Foundation of China (No. U1706221, 51922002, 51771025, and 51701171) and the Fundamental Research Funds for the Central Universities (FRF-TP-17-19-003C1Z). Author R. Shi would like to acknowledge the especial sponsor for the Research Student Attachment Programme from the graduate school of the University of Science and Technology Beijing.

References:

[1] Y.S. Chen, H. Lu, J. Liang, A. Rosenthal, H. Liu, G. Sneddon, I. McCarroll, Z. Zhao, W. Li, A. Guo, J.M. Cairney, Observation of hydrogen trapping at dislocations, grain boundaries, and precipitates, Science 367(6474) (2020) 171-175.

[2] R. Shi, Z. Wang, L. Qiao, X. Pang, Microstructure evolution of in-situ nanoparticles and its comprehensive effect on high strength steel, J. Mater. Sci. Technol. 35(9) (2019) 1940-1950.

[3] S. Zhang, E. Fan, J. Wan, J. Liu, Y. Huang, X. Li, Effect of Nb on the hydrogen-induced cracking of high-strength low-alloy steel, Corros. Sci. 139 (2018) 83-96.

[4] W.H. Johnson, On some remarkable changes produced in iron and steel by the action of hydrogen and acids, Proc. R. Soc. Lond. 23 (1874) 168–179.

[5] I.M. Robertson, P. Sofronis, A. Nagao, M.L. Martin, S. Wang, D.W. Gross, K.E. Nygren, Hydrogen embrittlement understood, Metall. Mater. Trans. A 46(6) (2015) 2323-2341.

[6] A.J. Breen, L.T. Stephenson, B. Sun, Y. Li, O. Kasian, D. Raabe, M. Herbig, B. Gault, Solute hydrogen and deuterium observed at the near atomic scale in high-strength steel, Acta Mater. 188 (2020) 108-120.

[7] Y.S. Chen, D. Haley, S.S. Gerstl, A.J. London, F. Sweeney, R.A. Wepf, W.M. Rainforth, P.A. Bagot, M.P. Moody, Direct observation of individual hydrogen atoms at trapping sites in a ferritic steel, Science 355(6330) (2017) 1196-1199.
[8] M. Nagumo, K. Takai, The predominant role of strain-induced vacancies in hydrogen embrittlement of steels: Overview, Acta Mater. 165 (2019) 722-733.
[9] L. Chen, X. Xiong, X. Tao, Y. Su, L. Qiao, Effect of dislocation cell walls on hydrogen adsorption, hydrogen trapping and hydrogen embrittlement resistance, Corros. Sci. 166 (2020) 108428.
[10] M.L. Martin, M. Dadfarnia, A. Nagao, S. Wang, P. Sofronis, Enumeration of the hydrogen-enhanced localized plasticity mechanism for hydrogen embrittlement in structural materials, Acta Mater. 165 (2019) 734-750.
[11] S. Wang, M.L. Martin, P. Sofronis, S. Ohnuki, N. Hashimoto, I.M. Robertson, Hydrogen-induced intergranular failure of iron, Acta Mater. 69 (2014) 275-282.
[12] A. Turk, G.R. Joshi, M. Gintalas, M. Callisti, P.E.J. Rivera-Díaz-del-Castillo, E.I. Galindo-Nava, Quantification of hydrogen trapping in multiphase steels: Part I – Point traps in martensite, Acta Mater. 194 (2020) 118-133.
[13] H. Asahi, D. Hirakami, S. Yamasaki, Hydrogen trapping behavior in vanadium-added steel, ISIJ Int. 43(4) (2003) 527-533.
[14] B. Malard, B. Remy, C. Scott, A. Deschamps, J. Chêne, T. Dieudonné, M.H. Mathon, Hydrogen trapping by VC precipitates and structural defects in a high strength Fe–Mn–C steel studied by small-angle neutron scattering, Mater. Sci. Eng. A 536 (2012) 110-116.
[15] T. Depover, K. Verbeken, Evaluation of the effect of V_4C_3 precipitates on the hydrogen induced mechanical degradation in Fe-C-V alloys, Mater. Sci. Eng. A 675 (2016) 299-313.

[16] A. Turk, D. San Martín, P.E.J. Rivera-Díaz-del-Castillo, E.I. Galindo-Nava, Correlation between vanadium carbide size and hydrogen trapping in ferritic steel, Scr. Mater. 152 (2018) 112-116.

[17] J. Takahashi, K. Kawakami, T. Tarui, Direct observation of hydrogen-trapping sites in vanadium carbide precipitation steel by atom probe tomography, Scr. Mater. 67(2) (2012) 213-216.

[18] J. Takahashi, K. Kawakami, Y. Kobayashi, Origin of hydrogen trapping site in vanadium carbide precipitation strengthening steel, Acta Mater. 153 (2018) 193-204.

[19] G.M. Pressouyre, I.M. Bernstein, A quantitative analysis of hydrogen trapping, Metall. Trans. A 9 (1978) 1571-1580.

[20] S.M. Lee, J.Y. Lee, The effect of the interface character of TiC particles on hydrogen trapping in steel, Acta Metall. 35 (1987) 2695-2700.

[21] F.G. Wei, K. Tsuzaki, Quantitative analysis on hydrogen trapping of TiC particles in steel, Metall. Mater. Trans. A 37(2) (2006) 331-353.

[22] A. Nagao, M.L. Martin, M. Dadfarnia, P. Sofronis, I.M. Robertson, The effect of nanosized (Ti,Mo)C precipitates on hydrogen embrittlement of tempered lath martensitic steel, Acta Mater. 74 (2014) 244-254.

[23] T. Depover, K. Verbeken, The effect of TiC on the hydrogen induced ductility loss and trapping behavior of Fe-C-Ti alloys, Corros. Sci. 112 (2016) 308-326.

[24] D. Di Stefano, R. Nazarov, T. Hickel, J. Neugebauer, M. Mrovec, C. Elsässer, First-principles investigation of hydrogen interaction with TiC precipitates in α-Fe, Phys. Rev. B 93(18) (2016) 184108.

[25] J. Takahashi, K. Kawakami, Y. Kobayashi, T. Tarui, The first direct observation of hydrogen trapping sites in TiC precipitation-hardening steel through atom probe tomography, Scr. Mater. 63(3) (2010) 261-264.

[26] M. Ohnuma, J.-i. Suzuki, F.-G. Wei, K. Tsuzaki, Direct observation of hydrogen trapped by NbC in steel using small-angle neutron scattering, Scr. Mater. 58(2) (2008) 142-145.
[27] S. Zhang, J. Wan, Q. Zhao, J. Liu, F. Huang, Y. Huang, X. Li, Dual role of nanosized NbC precipitates in hydrogen embrittlement susceptibility of lath martensitic steel, Corros. Sci. 164 (2020) 108345.
[28] E. Wallaert, T. Depover, M. Arafin, K. Verbeken, Thermal desorption spectroscopy evaluation of the hydrogen-trapping capacity of NbC and NbN precipitates, Metall. Mater. Trans. A 45(5) (2014) 2412-2420.
[29] F.G. Wei, T. Hara, K. Tsuzaki, Nano-preciptates design with hydrogen trapping character in high strength steel, Proceedings of the 2008 International Hydrogen Conference–Effects of Hydrogen on Materials, 2009, pp. 448–455.
[30] C. Hin, Y. Bréchet, P. Maugis, F. Soisson, Kinetics of heterogeneous dislocation precipitation of NbC in alpha-iron, Acta Mater. 56(19) (2008) 5535-5543.
[31] J. Kim, J.-G. Jung, D.-H. Kim, Y.-K. Lee, The kinetics of Nb(C,N) precipitation during the isothermal austenite to ferrite transformation in a low-carbon Nb-microalloyed steel, Acta Mater. 61(19) (2013) 7437-7443.
[32] J. Bian, H. Mohrbacher, H. Lu, W. Wang, Development of Press Hardening Steel with High Resistance to Hydrogen Embrittlement, HSLA Steels 2015, Microalloying 2015 & Offshore Engineering Steels 2015, 2016, pp. 571–576.
[33] L. Lin, B.-s. Li, G.-m. Zhu, Y.-l. Kang, R.-d. Liu, Effect of niobium precipitation behavior on microstructure and hydrogen induced cracking of press hardening steel 22MnB5, Mater. Sci. Eng. A 721 (2018) 38-46.
[34] B. Gault, M.P. Moody, J.M. Cairney, S.P. Ringer, Atom Probe Microscopy, Springer, New York, 2012.

[35] S. Echeverri Restrepo, D. Di Stefano, M. Mrovec, A.T. Paxton, Density functional theory calculations of iron–vanadium carbide interfaces and the effect of hydrogen, Int. J. Hydrogen Energy 45(3) (2020) 2382-2389.

[36] M.G. Akben, I. Weiss, J.J. Jonas, Dynamic precipitation and solute hardening in A V microalloyed steel and two Nb steels containing high levels of Mn, Acta Metall. 29(1) (1981) 111-121.

[37] T. Depover, K. Verbeken, The detrimental effect of hydrogen at dislocations on the hydrogen embrittlement susceptibility of Fe-C-X alloys: An experimental proof of the HELP mechanism, Int. J. Hydrogen Energy 43(5) (2018) 3050-3061.

[38] X.-S. Yang, S. Sun, H.-H. Ruan, S.-Q. Shi, T.-Y. Zhang, Shear and shuffling accomplishing polymorphic fcc $\gamma \rightarrow$ hcp $\varepsilon \rightarrow$ bct α martensitic phase transformation, Acta Mater. 136 (2017) 347-354.

[39] P. Hohenberg, W. Kohn, Inhomogeneous electron gas, Phys. Rev. 136(3B) (1964) 864-871.

[40] W. Kohn, L.J. Sham, Self-consistent equations including exchange and correlation effects, Phys. Rev. 140(4A) (1965) 1133-1138.

[41] G. Kresse, J. Hafner, Ab initio molecular dynamics for open-shell transition metals, Phys. Rev. B 48(17) (1993) 13115-13118.

[42] G. Kresse, J. Furthmuller, Efficient iterative schemes for ab initio total-energy calculations using a plane-wave basis set, Phys. Rev. B 54(16) (1996) 11169-11186.

[43] P.E. Blochl, Projector augmented-wave method, Phys. Rev. B 50(24) (1994) 17953-17979.

[44] J.P. Perdew, K. Burke, M. Ernzerhof, Generalized gradient approximation made simple, Phys. Rev. Lett. 77(18) (1996) 3865-3868.

[45] H. Stuart, N. Ridley, Thermal expansion of some carbides and tessellated stresses in steels, J. Iron Steel Inst. 208(12) (1970) 1087-1092.

[46] W.A. Counts, C. Wolverton, R. Gibala, First-principles energetics of hydrogen traps in α-Fe: Point defects, Acta Mater. 58(14) (2010) 4730-4741.
[47] G. Kurdjumov, G. Sachs, über den Mechanismus der Stahlhrtung, Zeit. F. Phys. 64 (1930) 325-343.
[48] U. Dahmen, Orientation relationships in precipitation systems, Acta Metall. 30(1) (1982) 63-73.
[49] X.L. Li, X.T. Deng, C.S. Lei, Z.D. Wang, New orientation relationship with low interfacial energy in MC/ferrite system observed in Nb-Ti bearing steel during isothermal quenching process, Scr. Mater. 163 (2019) 101-106.
[50] X.S. Yang, S. Sun, X.L. Wu, E. Ma, T.Y. Zhang, Dissecting the mechanism of martensitic transformation via atomic-scale observations, Sci. Rep. 4 (2014) 6141.
[51] X.-S. Yang, S. Sun, T.-Y. Zhang, The mechanism of bcc α′ nucleation in single hcp ε laths in the fcc γ → hcp ε → bcc α′ martensitic phase transformation, Acta Mater. 95 (2015) 264-273.
[52] S.S. Quek, Y. Xiang, D.J. Srolovitz, Loss of interface coherency around a misfitting spherical inclusion, Acta Mater. 59(14) (2011) 5398-5410.
[53] R.G. Baker, J. Nutting, Precipitation processes in steels, Iron and Steel Institute, Special Report 64 (1959) 1-22.
[54] F.-G. Wei, T. Hara, K. Tsuzaki, High-resolution transmission electron microscopy study of crystallography and morphology of TiC precipitates in tempered steel, Philos. Mag. 84(17) (2004) 1735-1751.
[55] P. Yu, Y. Cui, G.-z. Zhu, Y. Shen, M. Wen, The key role played by dislocation core radius and energy in hydrogen interaction with dislocations, Acta Mater. 185 (2020) 518-527.
[56] A. Drexler, T. Depover, S. Leitner, K. Verbeken, W. Ecker, Microstructural based hydrogen diffusion and trapping models applied to Fe–C–X alloys, J. Alloys Compd. 826 (2020) 154057.

[57] K. Kawakami, T. Matsumiya, Numerical analysis of hydrogen trap state by TiC and V_4C_3 in bcc-Fe, ISIJ Int. 52(9) (2012) 1693-1697.
[58] A. Drexler, T. Depover, K. Verbeken, W. Ecker, Model-based interpretation of thermal desorption spectra of Fe-C-Ti alloys, J. Alloys Compd. 789 (2019) 647-657.
[59] H.E. Kissinger, Reaction kinetics in differential thermal analysis, Anal. Chem. 29(11) (1957) 1702-1706.
[60] W.Y. Choo, J.Y. Lee, Thermal analysis of trapped hydrogen in pure iron, Metall. Trans. A 13(1) (1982) 135-140.
[61] M. Itakura, H. Kaburaki, M. Yamaguchi, T. Okita, The effect of hydrogen atoms on the screw dislocation mobility in bcc iron: A first-principles study, Acta Mater. 61(18) (2013) 6857-6867.
[62] X. Jin, L. Xu, W. Yu, K. Yao, J. Shi, M. Wang, The effect of undissolved and temper-induced (Ti,Mo)C precipitates on hydrogen embrittlement of quenched and tempered Cr-Mo steel, Corros. Sci. 166 (2020) 108421.
[63] Y.H. Fan, B. Zhang, H.L. Yi, G.S. Hao, Y.Y. Sun, J.Q. Wang, E.H. Han, W. Ke, The role of reversed austenite in hydrogen embrittlement fracture of S41500 martensitic stainless steel, Acta Mater. 139 (2017) 188-195.
[64] J. Sanchez, S.F. Lee, M.A. Martin-Rengel, J. Fullea, C. Andrade, J. Ruiz-Hervías, Measurement of hydrogen and embrittlement of high strength steels, Eng. Fail. Anal. 59 (2016) 467-477.
[65] A. Kuduzovic, M.C. Poletti, C. Sommitsch, M. Domankova, S. Mitsche, R. Kienreich, Investigations into the delayed fracture susceptibility of 34CrNiMo6 steel, and the opportunities for its application in ultra-high-strength bolts and fasteners, Mater. Sci. Eng. A 590 (2014) 66-73.
[66] J. Venezuela, Q. Liu, M. Zhang, Q. Zhou, A. Atrens, The influence of hydrogen on the mechanical and fracture properties of some martensitic

advanced high strength steels studied using the linearly increasing stress test, Corros. Sci. 99 (2015) 98-117.

[67] A. Nagao, M. Dadfarnia, B.P. Somerday, P. Sofronis, R.O. Ritchie, Hydrogen-enhanced-plasticity mediated decohesion for hydrogen-induced intergranular and “quasi-cleavage” fracture of lath martensitic steels, J. Mech. Phys. Solids 112 (2018) 403-430.

[68] R. Kirchheim, Revisiting hydrogen embrittlement models and hydrogen-induced homogeneous nucleation of dislocations, Scr. Mater. 62(2) (2010) 67-70.

[69] P. Novak, R. Yuan, B.P. Somerday, P. Sofronis, R.O. Ritchie, A statistical, physical-based, micro-mechanical model of hydrogen-induced intergranular fracture in steel, J. Mech. Phys. Solids 58(2) (2010) 206-226.

[70] S. Takebayashi, T. Kunieda, N. Yoshinaga, K. Ushioda, S. Ogata, Comparison of the dislocation density in martensitic steels evaluated by some X-ray diffraction methods, ISIJ Int. 50(6) (2010) 875-882.

[71] G.K. Williamson, W.H. Hall, X-ray line broadening from filed aluminium and wolfram, Acta Metall. 1 (1953) 22-31.

[72] H. Dogan, D. Li, J.R. Scully, Controlling hydrogen embrittlement in precharged ultrahigh-strength steels, Corrosion 63(7) (2007) 689-703.

[73] C.D. Beachem, A new model for hydrogen-assisted cracking (hydrogen “embrittlement”), Metall. Mater. Trans. B 3(2) (1972) 441-455.

[74] D. Guedes, L. Cupertino Malheiros, A. Oudriss, S. Cohendoz, J. Bouhattate, J. Creus, F. Thébault, M. Piette, X. Feaugas, The role of plasticity and hydrogen flux in the fracture of a tempered martensitic steel: A new design of mechanical test until fracture to separate the influence of mobile from deeply trapped hydrogen, Acta Mater. 186 (2020) 133-148.

[75] D. Pérez Escobar, T. Depover, E. Wallaert, L. Duprez, M. Verhaege, K. Verbeken, Thermal desorption spectroscopy study of the interaction between

hydrogen and different microstructural constituents in lab cast Fe–C alloys, Corros. Sci. 65 (2012) 199-208.

[76] J. Venezuela, E. Gray, Q. Liu, Q. Zhou, C. Tapia-Bastidas, M. Zhang, A. Atrens, Equivalent hydrogen fugacity during electrochemical charging of some martensitic advanced high-strength steels, Corros. Sci. 127 (2017) 45-58.

Figure 1

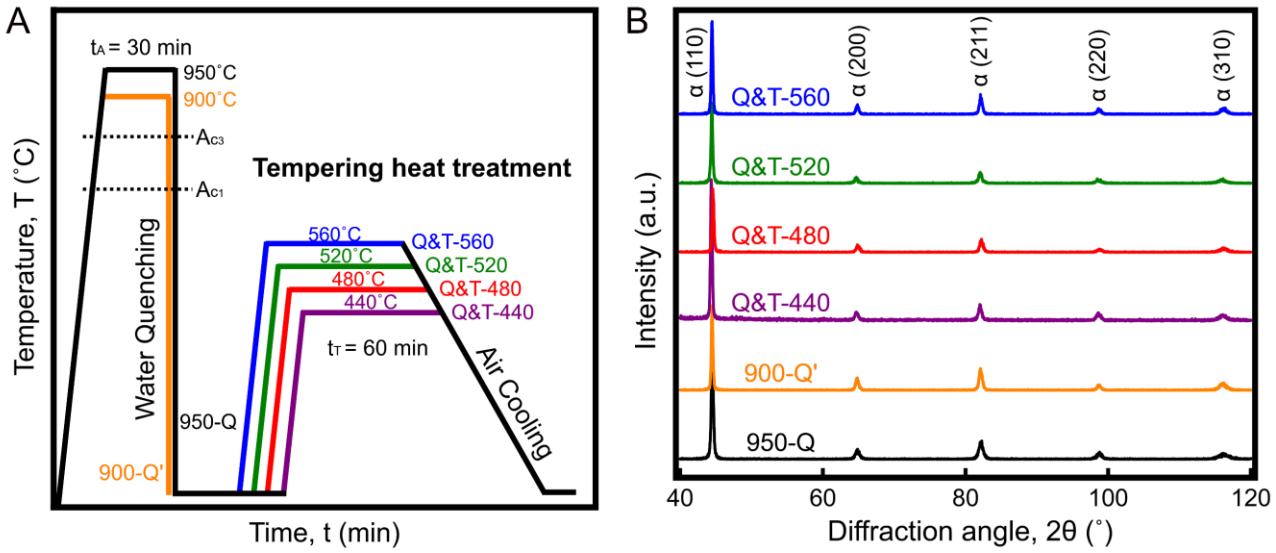

Fig. 1. (A) Schematic of the heat-treatment procedures. (B) XRD profiles of the steels after various heat treatments. All samples are composed entirely of single-phase bcc martensite.

Figure 2

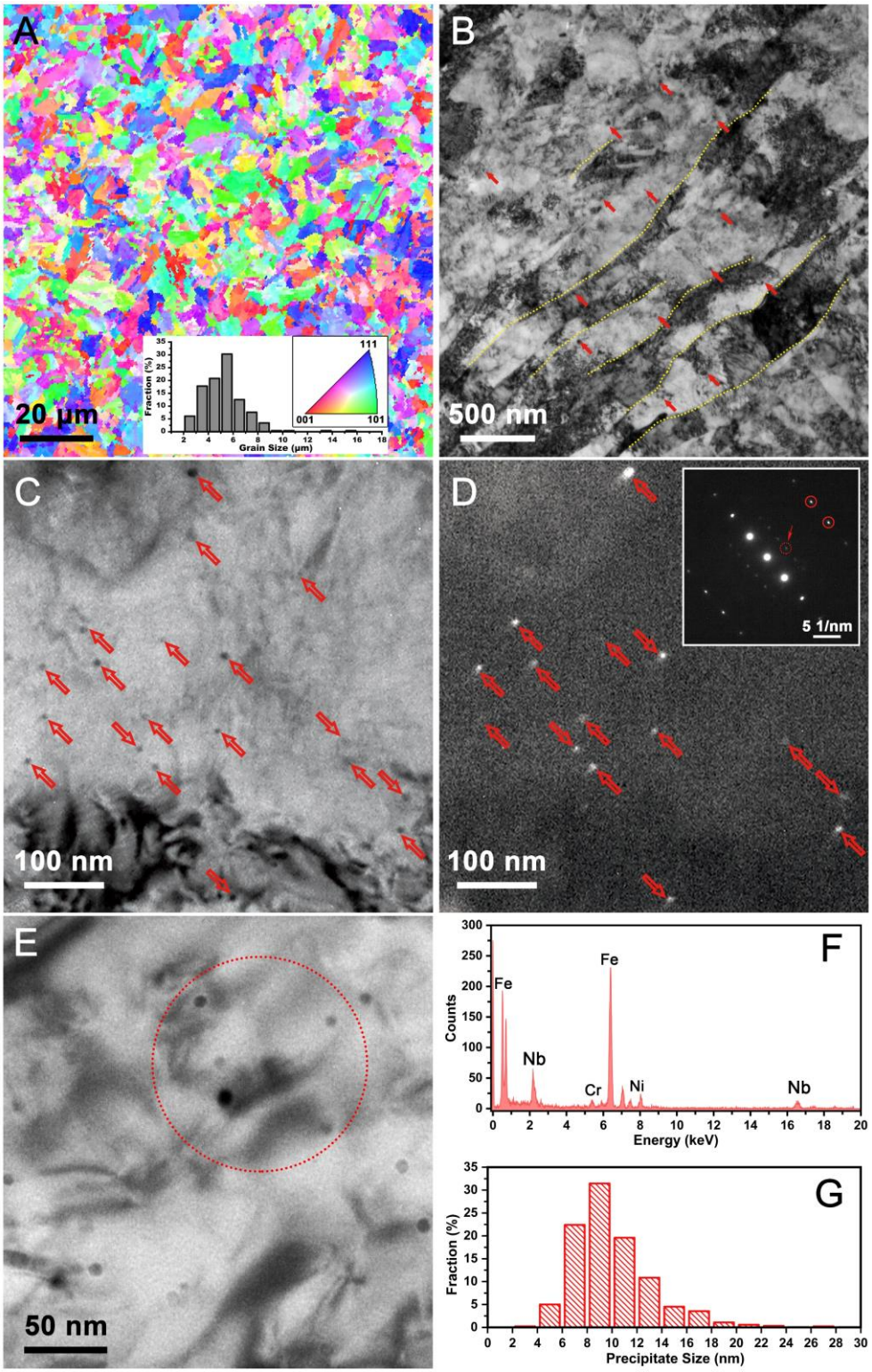

Fig. 2. Microstructural characterization of the investigated Q&T-480: (A) EBSD image showing the microstructure of the equiaxed grains, with the grain size distribution in the inset. (B) Representative TEM image showing the distribution of martensite laths (yellow broken lines) and nanoprecipitates (arrows). The bright-field (C) and corresponding dark-field (D) TEM images showing nanoprecipitates dispersed in the matrix, with associated selected-area diffraction patterns in the inset. (E) Enlarged view of the distribution of nanoprecipitates. (F) EDS analysis results corresponding to the dashed circle in (E). (G) Size distribution of the nanoprecipitates.

Figure 3

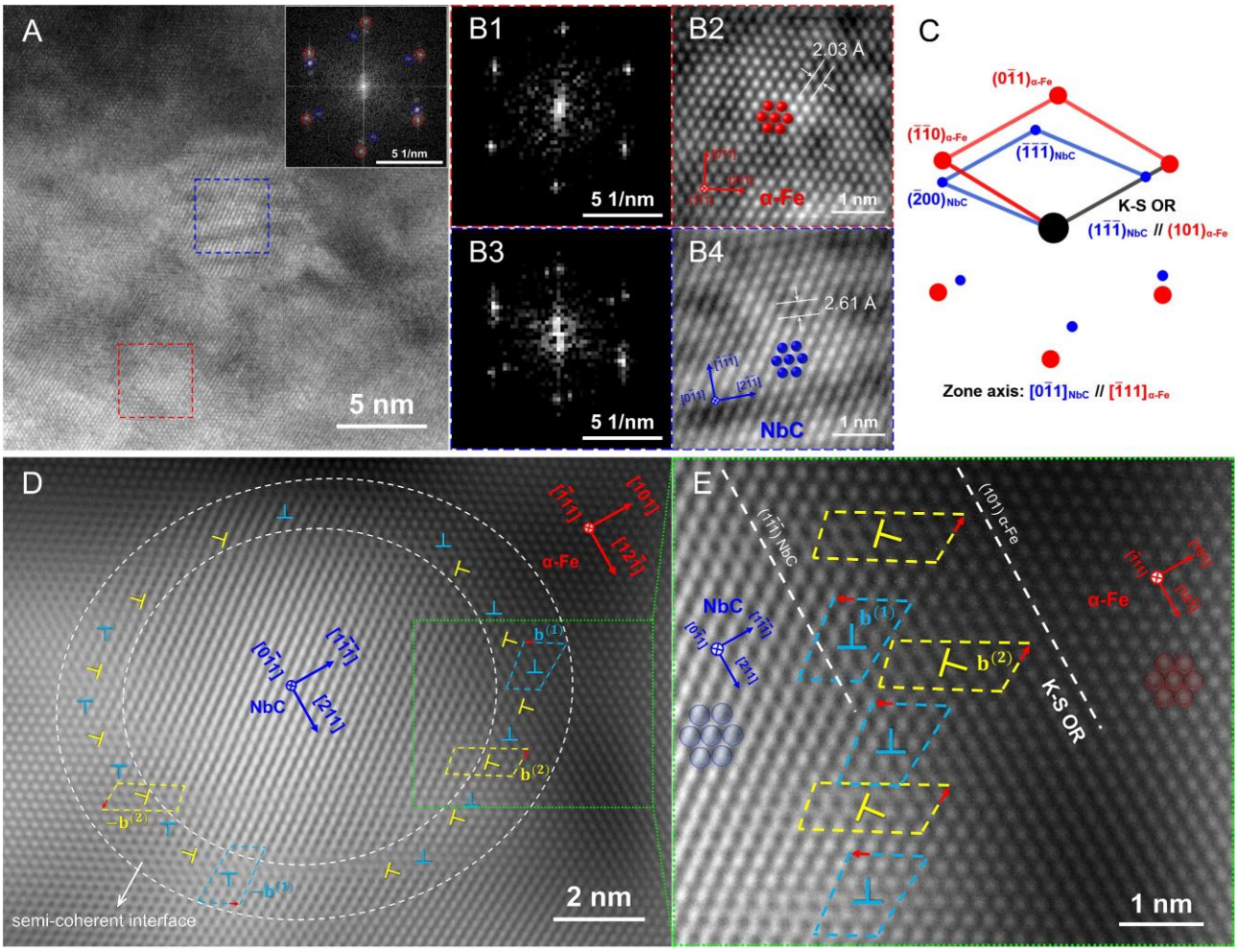

Fig. 3. HRTEM observations of misfit dislocations at a NbC/α-Fe semi-coherent interface along the $[0\bar{1}1]_{NbC}$ // $[\bar{1}11]_{\alpha\text{-}Fe}$ directions in Q&T-480. (A) HRTEM image of a typical NbC and the surrounding α-Fe; the corresponding FFT patterns are indicated in the inset. (B1) FFT and (B2) IFFT of the red dashed box from (A), indicating the bcc α-Fe along [$\bar{1}$11]. (B3) FFT and (B4) IFFT of the blue dashed box from (A) indicating the fcc NbC along [0$\bar{1}$1]. (C) Schematic summarizing the diffraction patterns from (A) for the orientation relationship (OR) between the NbC and α-Fe, showing $(1\bar{1}\bar{1})_{NbC}$ // $(101)_{\alpha\text{-}Fe}$ with Kurdjumov–Sachs (K–S) OR. (D) Interfacial structure for the NbC/α-Fe interface, showing the high-density misfit dislocations. The dislocations are indicated by the "⊥" symbols, and the Burgers vectors are depicted by Burgers circuits (dashed circuits). (E) Enlarged image corresponding to the green dotted zone in (D).

Figure 4

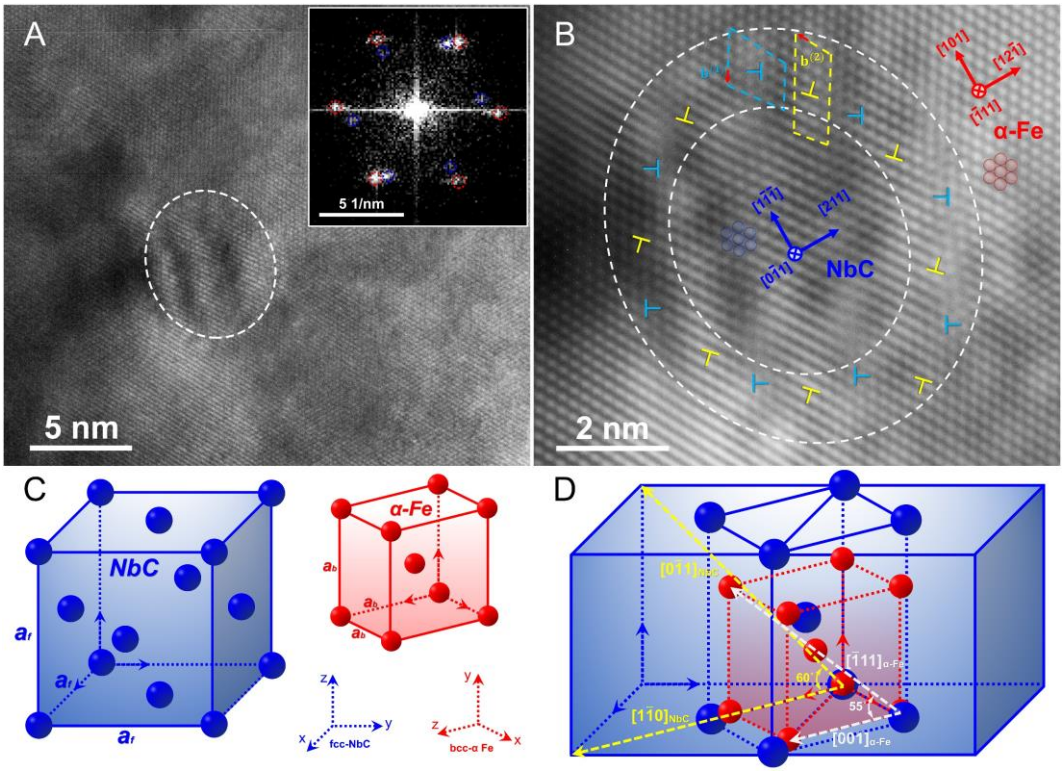

Fig. 4. HRTEM observation of misfit dislocations at a NbC/α-Fe semi-coherent interface and schematic of the lattice correspondence for the NbC and α-Fe in Q&T-480. (A) HRTEM image of a small NbC and surrounding α-Fe; the corresponding FFT patterns are shown in the inset. (B) Interfacial structure for the NbC/α-Fe interface, showing the two sets of misfit dislocations with 4 $\mathbf{b}^{(1)}$ and 4 $\mathbf{b}^{(2)}$. (C) The defined crystallographic coordinate system for fcc NbC (blue) and bcc α-Fe (red) structures. (D) Lattice correspondence for the NbC and α-Fe show that when $[\bar{1}11]_{\alpha\text{-Fe}}$ rotated to $[001]_{\alpha\text{-Fe}}$, the $[0\bar{1}1]_{NbC}$ could not rotate to $[1\bar{1}0]_{NbC}$ (with inclined angle of at least 5°).

Figure 5

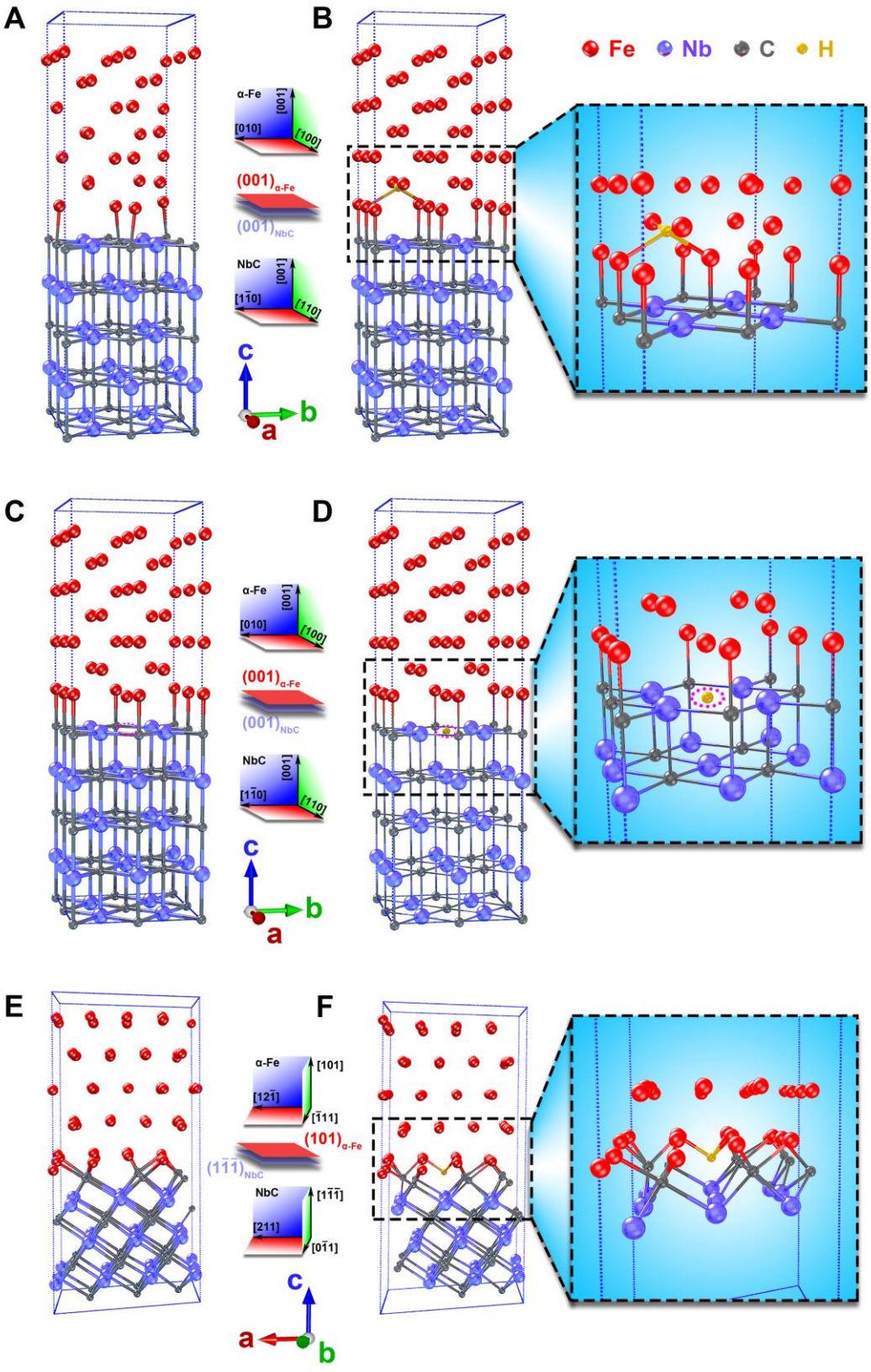

Fig. 5. Atomic structures in different NbC/α-Fe interfaces, as determined by DFT calculations. The (001) NbC/α-Fe coherent interface with the B–N OR (A) before and (B) after hydrogen segregation. The (001) NbC/α-Fe coherent interface with a surface carbon vacancy (C) before and (D) after hydrogen segregation. The NbC/α-Fe semi-coherent interface with the K–S OR (E) before and (F) after hydrogen segregation.

Figure 6

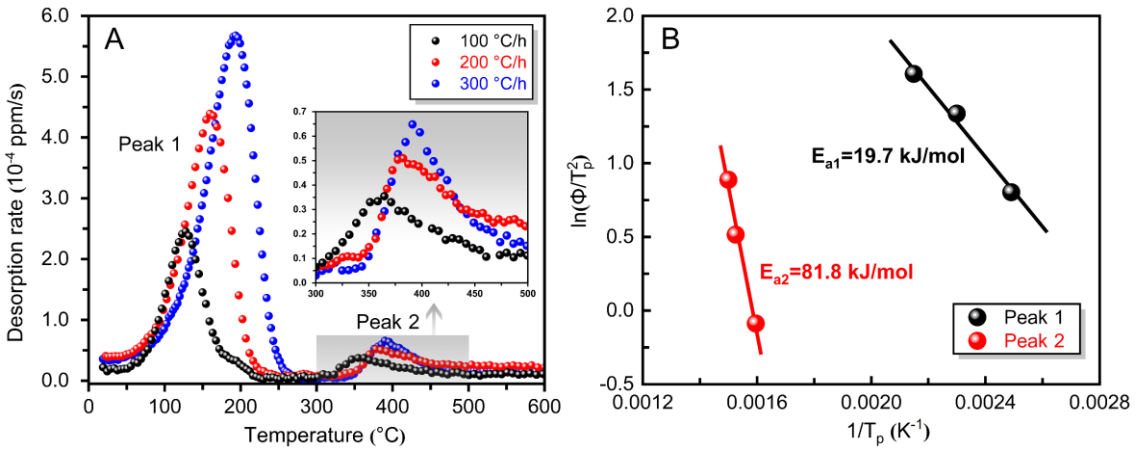

Fig. 6. Determination of the deep hydrogen trapping of NbC in the Q&T-480. (A) TDS profiles at different heating rates, with Peak 2 shown in the enlarged inset. (B) Plot of $\ln(\phi/T_p^2)$ as a function of $1/T_p$ to obtain the activation energy for hydrogen desorption, E_a.

Figure 7

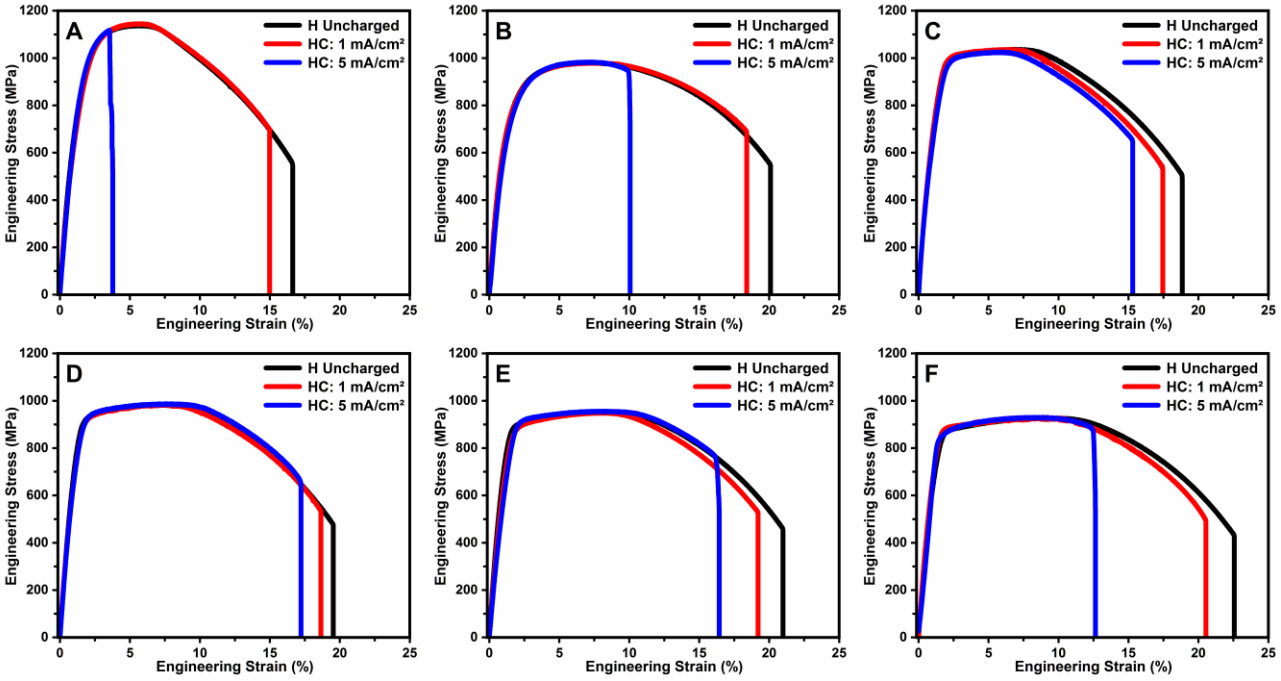

Fig. 7. Engineering stress–strain curves for SSRT tests of hydrogen uncharged samples (H Uncharged) and samples hydrogen pre-charged (HC) at 1 mA/cm^2 and 5 mA/cm^2 for 10 h: (A) 950-Q, (B) 900-Q′, (C) Q&T-440, (D) Q&T-480, (E) Q&T-520, and (F) Q&T-560.

Figure 8

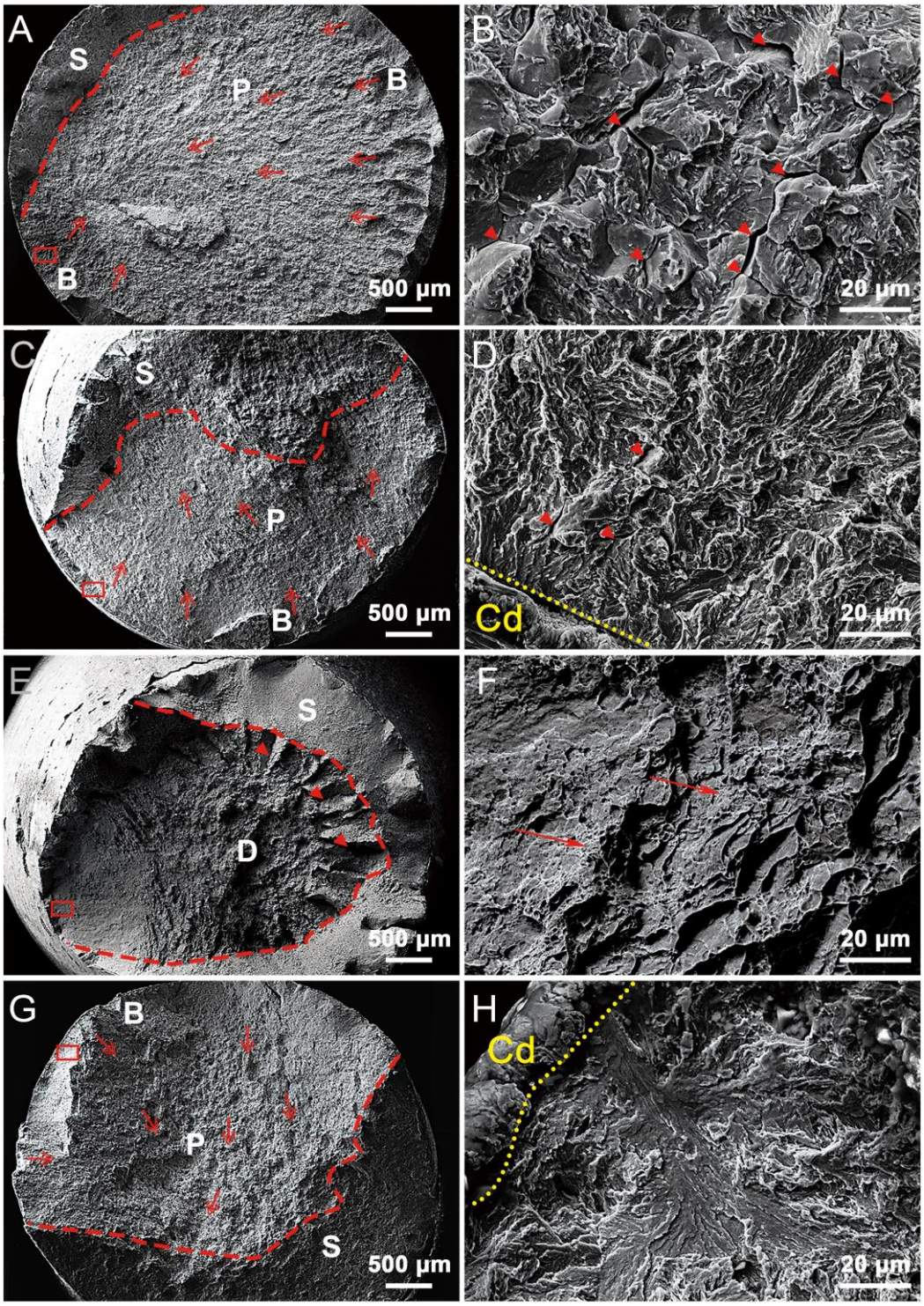

Fig. 8. Respective SEM micrographs of fracture surfaces of (A, B) 950-Q, (C, D) 900-Q′, (E, F) Q&T-480, and (G, H) Q&T-560, pre-charged at 5 mA/cm^2 for 10 h. (B), (D), (F), and (H) show enlarged views of the solid-line boxes in (A), (C), (E), and (G), respectively. Region “B” represents typical brittle crack initiation, and region “D” represents typical ductile crack initiation. Region “P” represents the crack propagation region, whereas the periphery in region “S” is the shear lip region. “Cd” indicates the electroplated layer of cadmium.

Figure 9

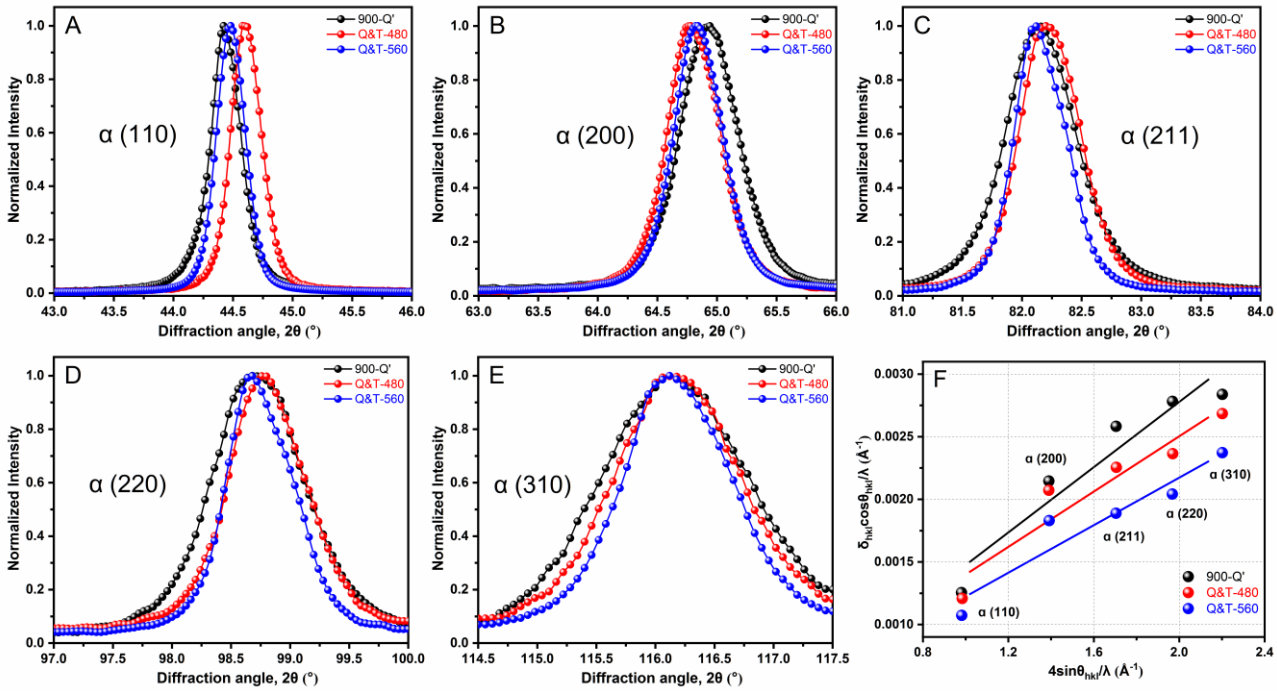

Fig. 9. XRD profiles for the determination of dislocation densities in the 900-Q′, Q&T-480, and Q&T-560 steels. (A), (B), (C), (D), and (E) are XRD profiles corresponding to the (110), (200), (211), (220), and (310) planes, respectively. (F) Williamson–Hall plots to determine the dislocation density.

Figure 10

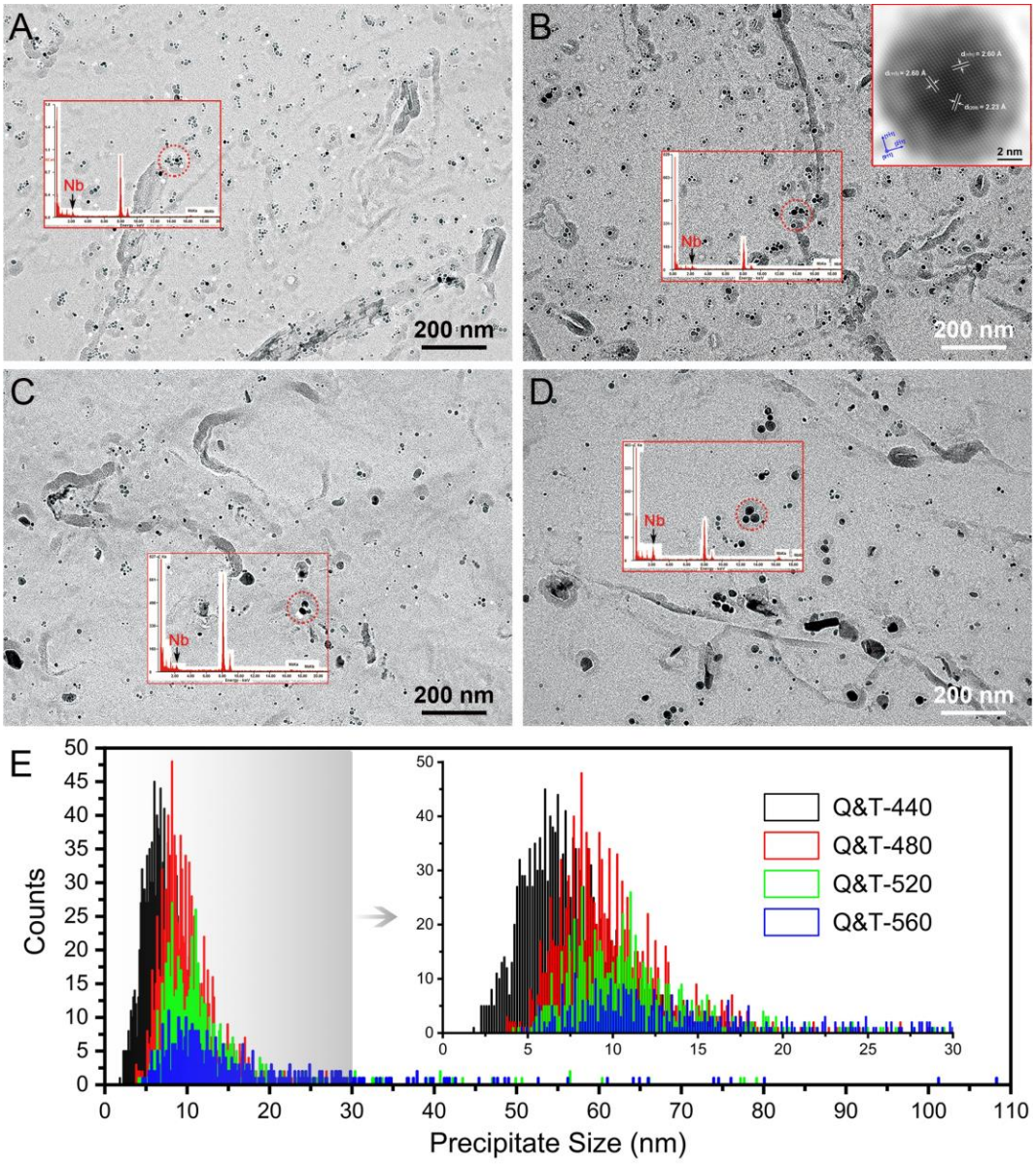

Fig. 10. Representative TEM images of nanoprecipitates showing the presence and distribution of nanoprecipitates in the tempered steels by carbon extraction replicas. (A) Q&T-440, (B) Q&T-480, (C) Q&T-520, and (D) Q&T-560. The corresponding EDS spectra taken from the nanoparticles are indicated by the red dashed circles. The HRTEM image of one nanoparticle in the Q&T-480, viewed along the $[011]_{NbC}$ direction, is presented in the inset of (B). (E) The carbide size distribution; the inset shows the distribution of particles with a diameter within 30 nm.

Figure 11

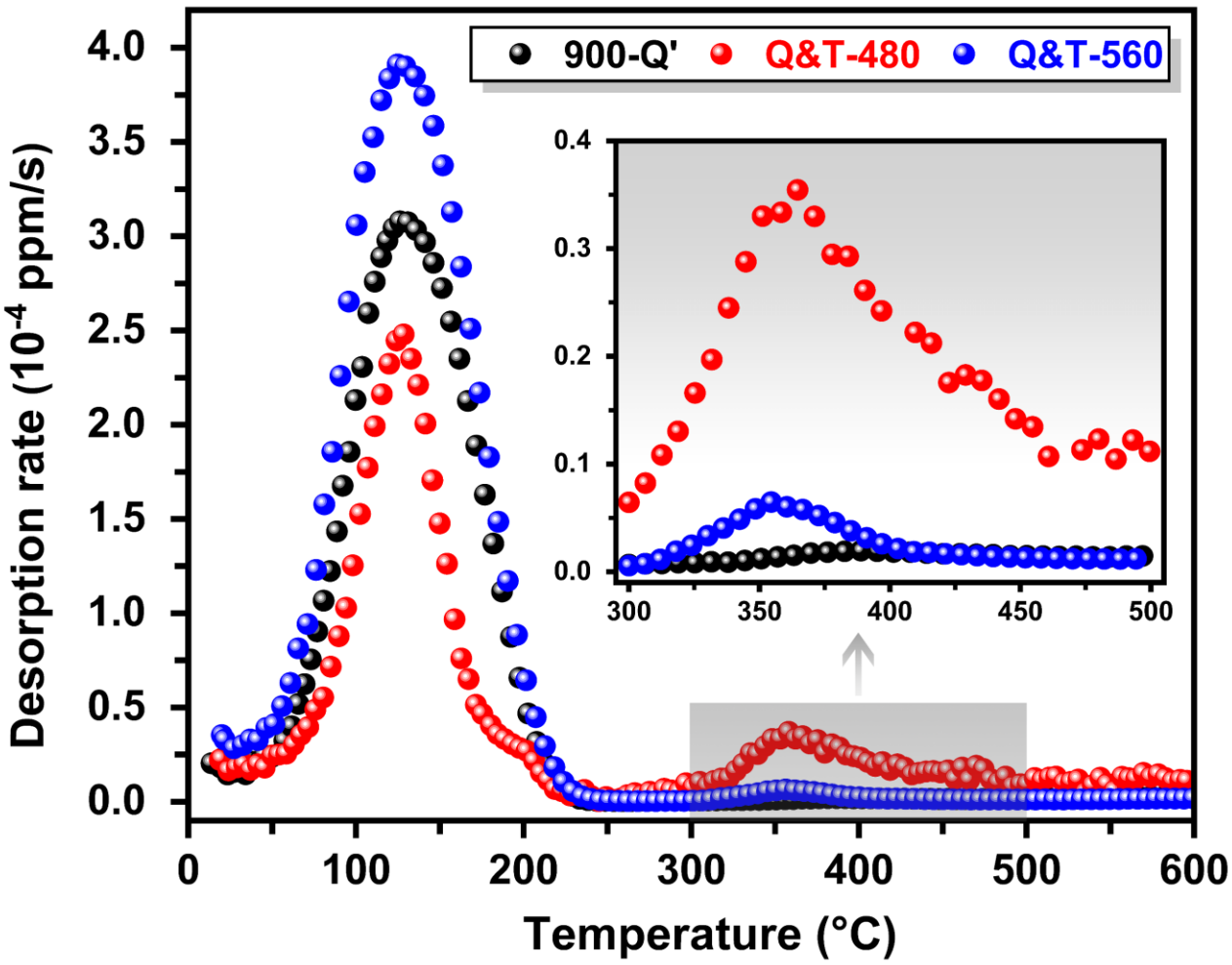

Fig. 11. The hydrogen desorption curves of 900-Q′, Q&T-480, and Q&T-560 steels hydrogen pre-charged at 5 mA/cm^2 for 10 h. The heating rate was 100 °C/h from ambient temperature to 600 °C. The TDS profiles corresponding to the temperature range from 300 °C to 500 °C are shown in the enlarged inset.

Figure 12

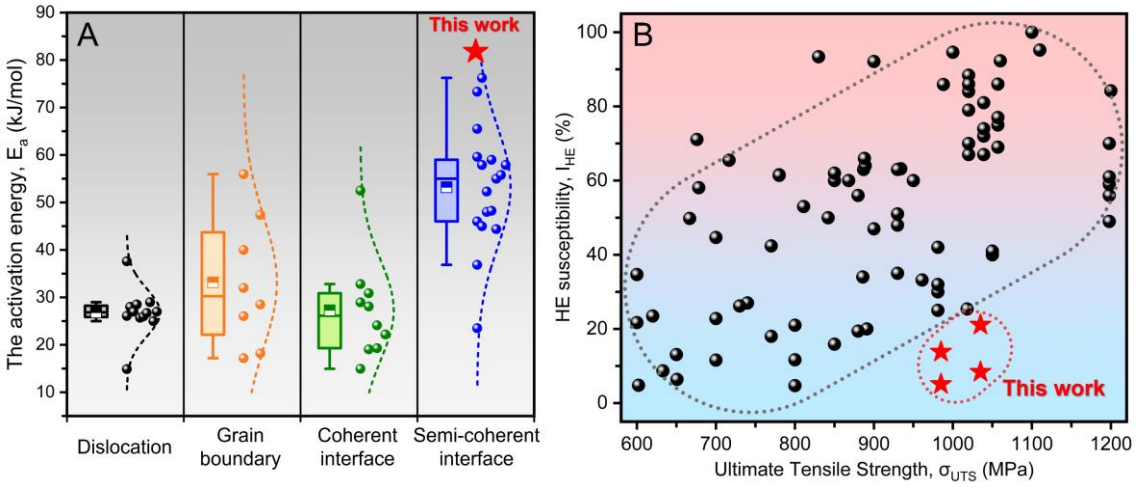

Fig. 12. Comparison of the hydrogen trapping ability and HE resistance of the samples investigated in this work and those investigated in previous studies. (A) Map of the hydrogen activation energy, E_a, versus different hydrogen traps (dislocations, grain boundaries, coherent interfaces, and semi-coherent interfaces of nanoprecipitates). (B) Map of HE susceptibility versus the ultimate tensile strength of high-strength steels in previous studies and in this work (Q&T-440 and Q&T-480 are indicated). The activation energy and HE susceptibility data corresponding to these reported studies were acquired from Supplementary Table S1 and Table S2.

Figure 13

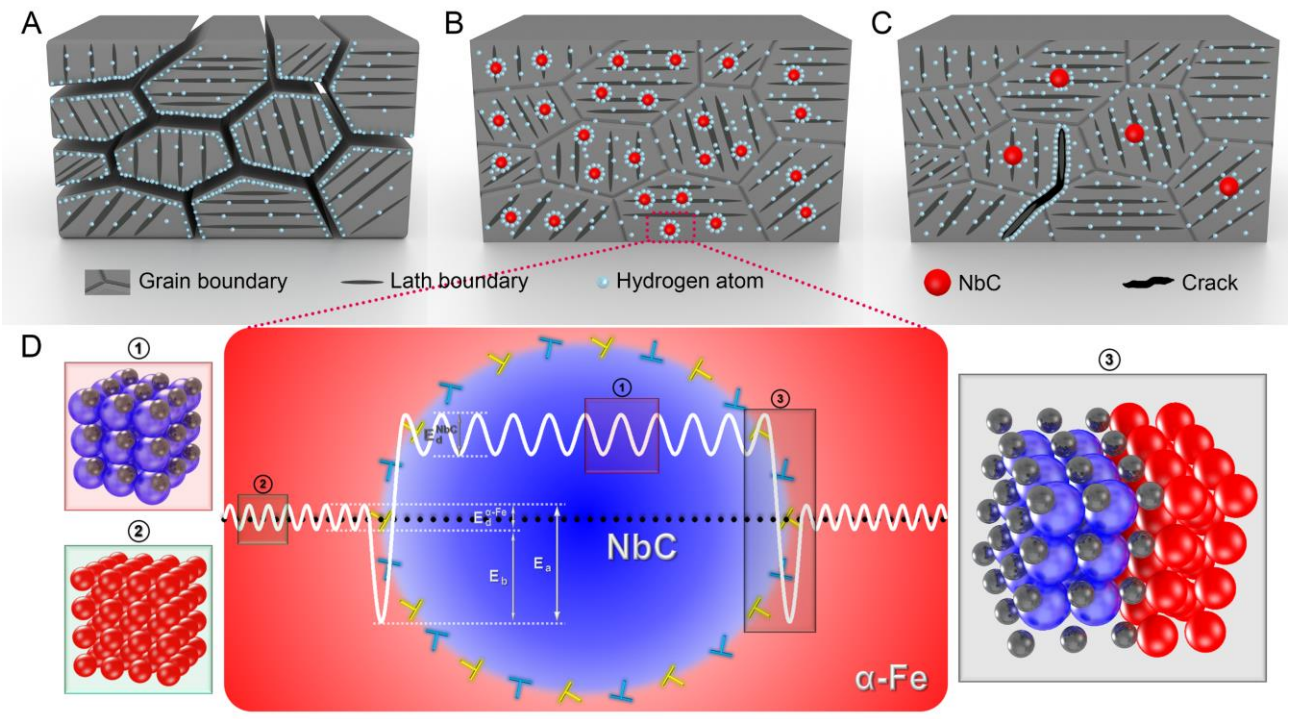

Fig. 13. Schematics showing the correlation between HE and deep hydrogen trapping in high-strength steels: (A) as-quenched steels without NbC nanoprecipitates, (B) tempered steels with uniformly dispersed dense NbC nanoprecipitates, and (C) tempered steels with few coarsened NbC nanoprecipitates. (D) Schematic of the deep hydrogen trapping in the NbC/α-Fe semi-coherent interface.

Table 1

Table 1 Summary of characteristic binding energies between hydrogen and different typical interfaces in this work and previous works.

Interface type	Binding energies (Calc), eV	Binding energies (Refs.), eV
Coherent interface	0.19	TiC: 0.18 [24], 0.25 [23] VC: 0.16 [57]
Coherent interface with surface carbon vacancy	0.33	TiC: 0.46 [24], 0.59 [58] VC: 0.38 [35]
Semi-coherent interface	0.80	TiC: 0.50 [24]

Table 2

Table 2 The evaluated mechanical properties for various hydrogen pre-charging conditions in the investigated steels. σ_{UTS}, δ, I_{HE}, and C_H are ultimate tensile strength, elongation, HE index, and hydrogen concentration, respectively.

Mechanical properties		950-Q	900-Q′	Q&T-440	Q&T-480	Q&T-520	Q&T-560
H Uncharged (Air)	σ_{UTS} (MPa)	1140±36	983±28	1035±23	985±20	950±16	930±12
	δ_0 (%)	15.70±1.04	19.12±1.26	17.97±1.13	18.70±0.61	20.16±0.68	21.82±1.46
H pre-charged (1 mA/cm^2, 10h)	δ_1 (%)	13.80±0.56	17.17±1.55	16.46±0.54	17.75±0.71	18.22±0.77	19.61±0.74
	I_{HE1} (%)	12.1±3.6	10.2±3.1	8.4±2.9	5.1±3.8	9.6±3.8	10.1±3.4
	C_H (ppm)	1.5±0.3	2.4±0.5	2.2±0.5	3.0±0.8	3.2±0.7	3.5±0.8
H pre-charged (5 mA/cm^2, 10h)	δ_2 (%)	1.67±1.02	8.24±0.38	14.17±0.98	16.12±0.51	14.91±1.12	10.96±1.09
	I_{HE2} (%)	89.4±7.1	56.9±2.4	21.1±5.4	13.8±2.7	26.0±5.6	49.8±5.0
	C_H (ppm)	4.6±0.8	4.7±0.6	4.9±0.8	5.1±0.9	5.4±1.1	5.5±0.8

Supplementary material for

Atomic-scale investigation of deep hydrogen trapping in NbC/α-Fe semi-coherent interfaces

Rongjian Shi [a, b], Yuan Ma [a, b], Zidong Wang [c], Lei Gao [a, b], Xu-Sheng Yang [d, e], Lijie Qiao [a, b, *], Xiaolu Pang [a, c, *]

[a] *Beijing Advanced Innovation Center for Materials Genome Engineering, University of Science and Technology Beijing, Beijing 100083, China*

[b] *Corrosion and Protection Center, University of Science and Technology Beijing, Beijing 100083, China*

[c] *School of Materials Science and Engineering, University of Science and Technology Beijing, Beijing 100083, China*

[d] *Advanced Manufacturing Technology Research Centre, Department of Industrial and Systems Engineering, The Hong Kong Polytechnic University, Hung Hom, Kowloon, Hong Kong, China*

[e] *Hong Kong Polytechnic University Shenzhen Research Institute, Shenzhen 518057, China*

* Corresponding authors.

E-mail addresses:

lqiao@ustb.edu.cn (L. Qiao), pangxl@mater.ustb.edu.cn (X. Pang).

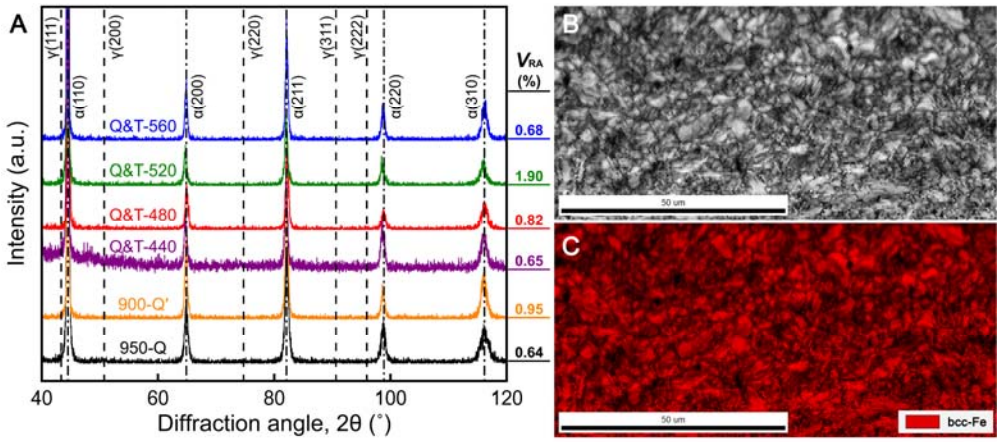

Fig. S1. (A) XRD profiles of the steels after various heat treatments. All samples are composed entirely of bcc-Fe and the amount of retained austenite (RA) is below the detection limit (3–5%) [1, 2]. EBSD characterization of the microstructure in Q&T-480 sample: (B) image quality (IQ) map and (C) phase map.

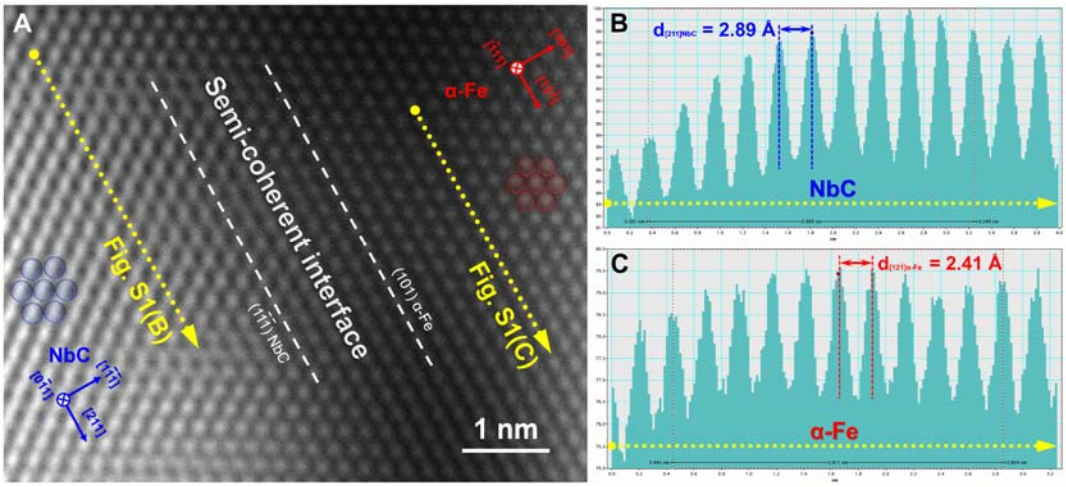

Fig. S2. (A) HRTEM image of the NbC/α-Fe interface region along the $[0\bar{1}1]_{NbC}$ // $[\bar{1}11]_{\alpha\text{-}Fe}$ directions in Q&T-480. (B–C) The representative atomic-scale intensity profiles for the atomic planar spacings of NbC and α-Fe in (A), respectively. The lattice misfit strain, *f*, between $[211]_{NbC}$ and $[12\bar{1}]_{\alpha\text{-}Fe}$ is $f = 100\% \times (d_{[211]NbC} - d_{[12\bar{1}]\alpha\text{-}Fe})/d_{[211]NbC} = 100\% \times (2.89\ Å - 2.41\ Å)/2.89\ Å = 16.61\%$.

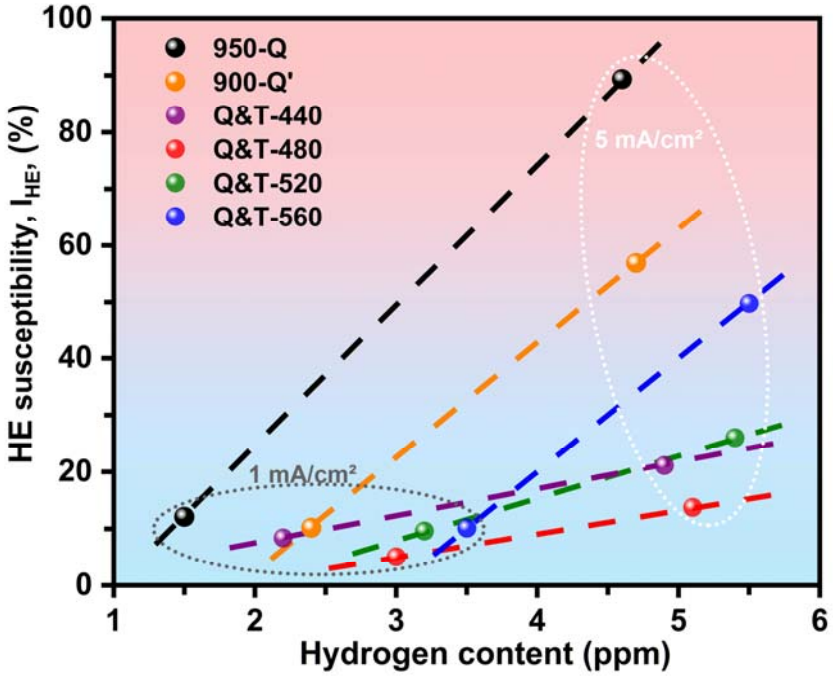

Fig. S3. The relationship between HE susceptibility, I_{HE}, and hydrogen content. The hydrogen content was measured by G4 PHOENIX at 800 °C for 20 min after hydrogen charging.

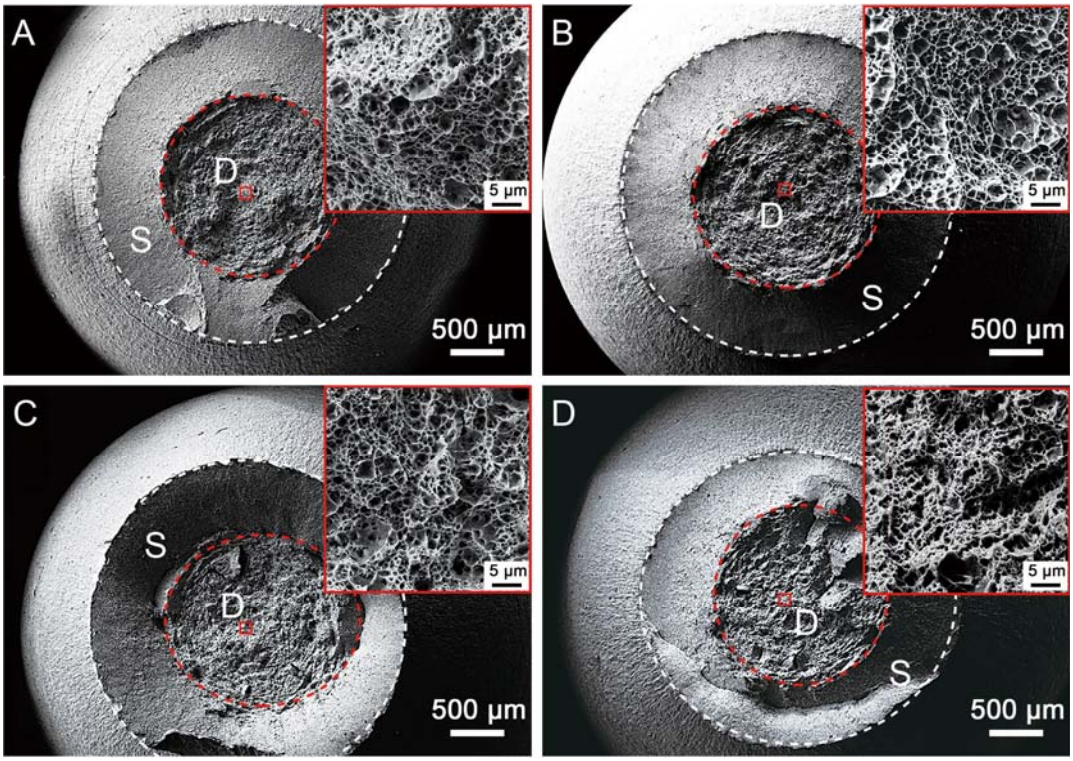

Fig. S4. SEM fractographs showing the top view of typical ductile fracture

surfaces of (A) 950-Q, (B) 900-Q′, (C) Q&T-480, and (D) Q&T-560 tested in air; the insets show the magnified views of the solid-line box. The central region “D” represents the typical ductile crack initiation and growth region, whereas the periphery in region “S” is the shear lip region.

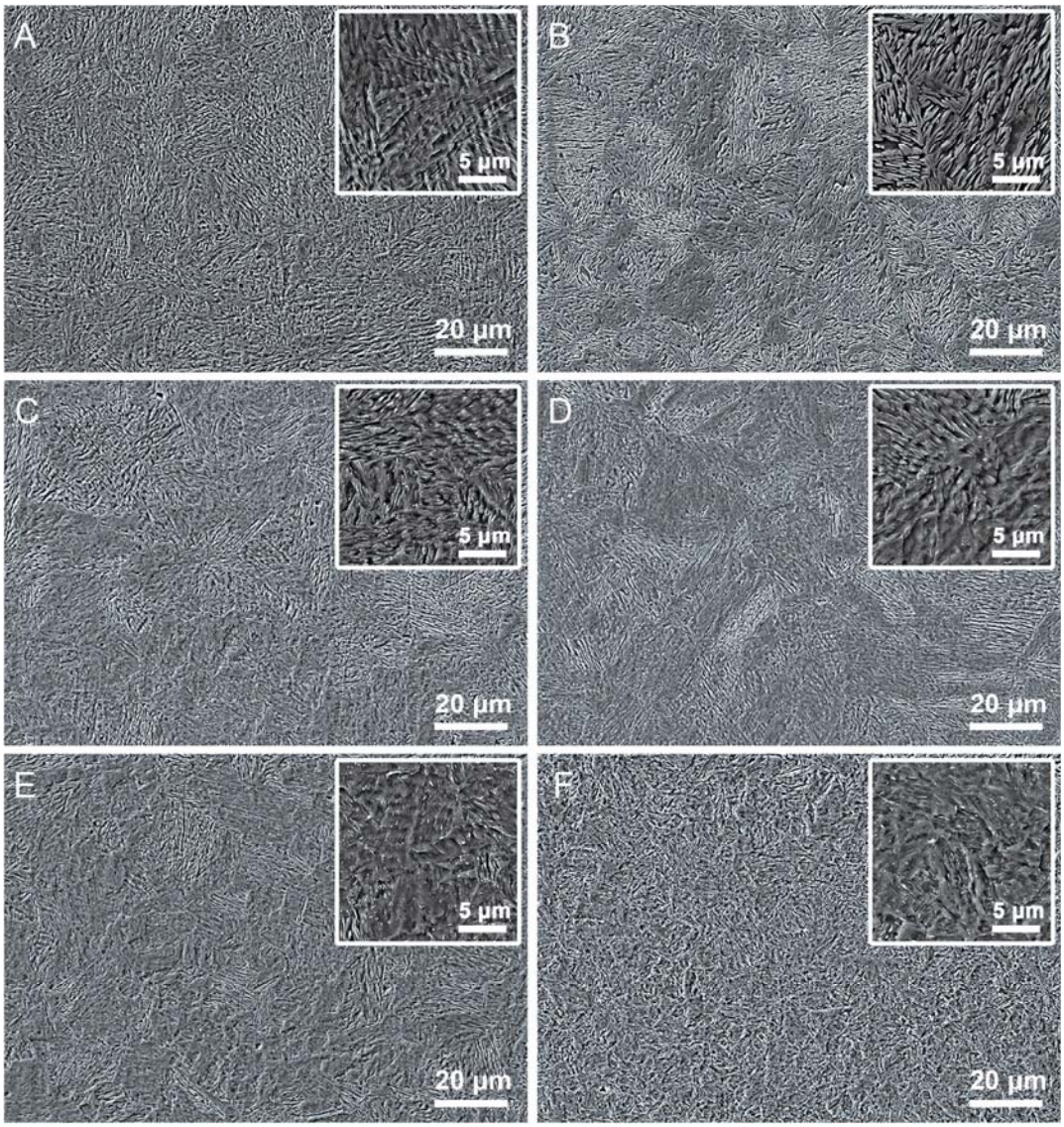

Fig. S5. Representative SEM images of microstructures of (A) 950-Q, (B) 900-Q′, (C) Q&T-440, (D) Q&T-480, (E) Q&T-520, and (F) Q&T-560. The morphology and distribution of martensite are indicated in the enlarged insets. After quenching and tempering, the Q&T steels are composed entirely of tempered martensite.

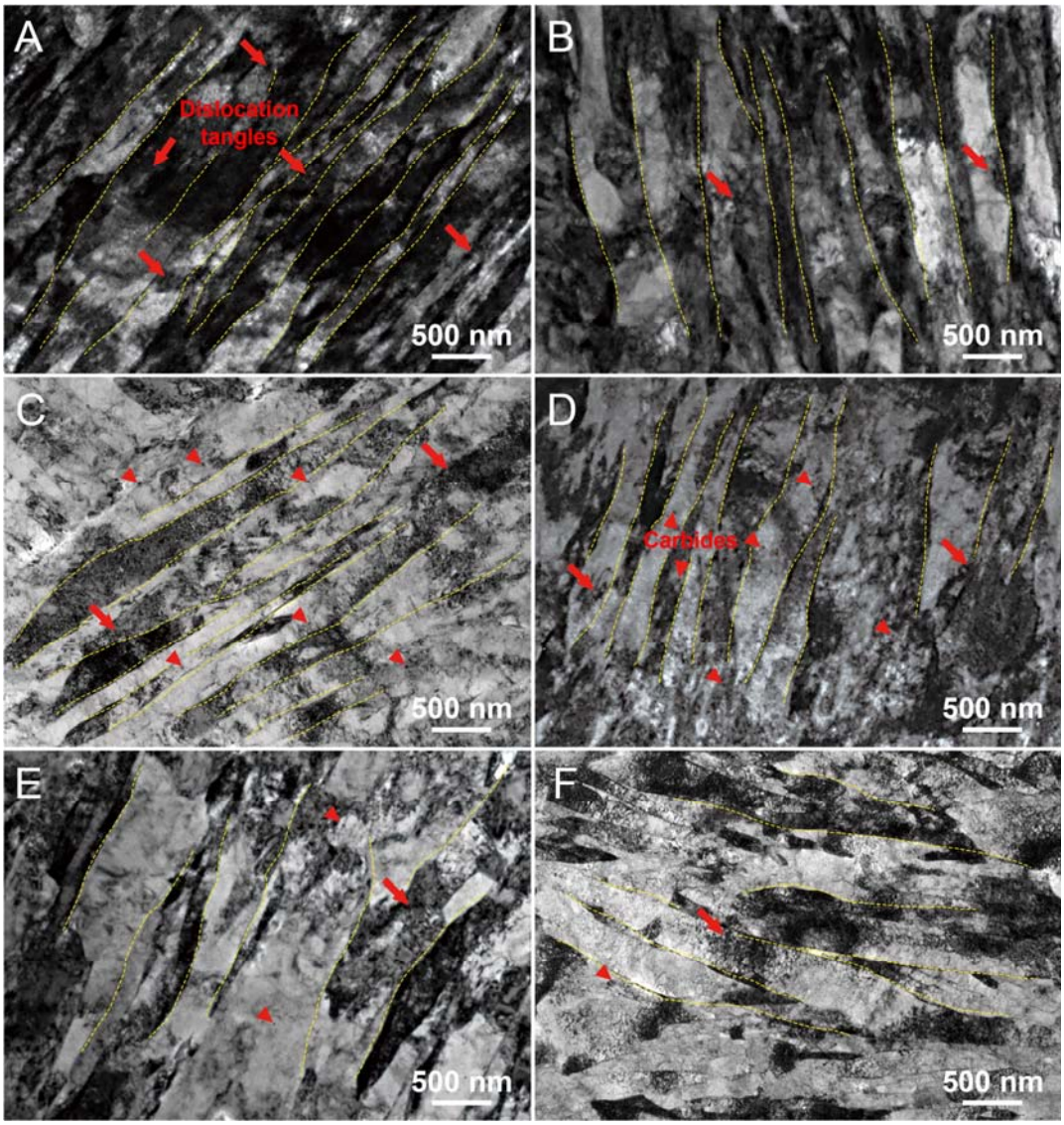

Fig. S6. TEM bright-field micrographs showing the overall microstructure of the martensite lath distribution: (A) 950-Q, (B) 900-Q′, (C) Q&T-440, (D) Q&T-480, (E) Q&T-520, and (F) Q&T-560. The yellow dashed lines indicate the martensite lath boundaries. The tangled dislocations are marked by arrows, showing the decrease of dislocation density with increasing tempering temperature. The arrowheads indicate the nanoprecipitates.

Table S1 Summary of typical hydrogen traps (dislocations, grain boundaries, coherent interfaces, and semi-coherent interfaces of nanoprecipitates) and the corresponding hydrogen activation energy, E_a, reported in previous studies.

Trap type	E_a, kJ/mol	Refs.	Trap type	E_a, kJ/mol	Refs.
Dislocation	14.9	[3]	Coherent: TiC	28.1	[4]
Dislocation	26.1	[5]	Coherent: TiC	52.5	
Dislocation	28.0	[6]	Coherent: TiC	19.3	[7]
Dislocation	27.0	[8]	Coherent: TiC	30.9	
Dislocation	28.5	[9]	Coherent: TiC	24.1	[10]
Dislocation	25.7	[11]	Coherent: TiC	22.2	[12]
Dislocation	26.0	[13]	Semi-coherent: VC	59.6	[14]
Dislocation	26.7		Semi-coherent: VC	36.9	[15]
Dislocation	37.6		Semi-coherent: VC	57.9	[10]
Dislocation	29.0	[16]	Semi-coherent: VC	73.3	
Dislocation	25.0	[17]	Semi-coherent: TiC	52.3	[18]
Dislocation	27.0	[18]	Semi-coherent: TiC	46.0	[4]
Grain boundary	26.1	[19]	Semi-coherent: TiC	59.0	
Grain boundary	57.0	[11]	Semi-coherent: TiC	45.0	[20]
Grain boundary	17.2	[21]	Semi-coherent: TiC	48.0	[22]
Grain boundary	40.0	[9]	Semi-coherent: TiC	55.0	[23]
Grain boundary	47.4	[11]	Semi-coherent: TiC	55.8	[18]
Grain boundary	28.5	[24]	Semi-coherent: TiC	48.3	[7]
Grain boundary	32.0	[19]	Semi-coherent: TiC	44.4	
Grain boundary	18.2	[21]	Semi-coherent: TiC	57.9	[10]
Coherent: VC	32.8	[10]	Semi-coherent: TiC	76.2	
Coherent: VC	15.0	[22]	Semi-coherent: NbC	23.5	[25]
Coherent: TiC	29.0		Semi-coherent: NbN	65.5	
Coherent: TiC	19.1	[26]			

Table S2 Summary of the ultimate tensile strength, σ_{UTS}, and the corresponding HE susceptibility, I_{HE}, of high-strength steels in previous studies. Data from the past five years in recent references were randomly selected here.

σ_{UTS}, MPa	I_{HE}, %	Refs.	σ_{UTS}, MPa	I_{HE}, %	Refs.
887	63	[27]	780	61.4	[28]
891	20		770	42.4	
886	34		1000	94.6	[29]
850	60	[5]	1020	88.4	
950	60		900	92.1	
1050	40		830	93.4	
934	63.2	[30]	770	18	[20]
676	71.1		842	50	
600	21.7	[31]	800	21	
650	13.1		868	60	
700	11.6		811	53	
620	23.5	[32]	888	66	
700	22.8		930	35	[33]
988	85.9	[34]	930	48	
961	33.2		930	51	
1018	25.4	[35]	930	63	
889	64		1057	69	
1200	84.2	[36]	1057	75	
1110	95.2		1057	77	
666.8	49.8	[37]	1057	86	
650.7	6.4		1039	67	
1100	100	[38]	1039	72	
678.3	58.08	[39]	1039	74	
716.7	65.48		1039	81	

740	27	[40]	1198	42	[33]
850	62		1198	49	
880	56		1198	56	
900	47		1198	59	
600	34.68	[41]	1198	61	
700	44.65		1198	70	
780	61.58		1020	67	
730	26.2	[42]	1020	70	
633	8.7		1020	79	
602	4.8		1020	84	
800	4.7	[43]	1020	86	
800	11.7		981	25	
1050	41		981	30	
880	19.4		981	32	
850	15.9		981	42	
1060	92.3				

References:

[1] M. Fantauzzi, C. Licheri, D. Atzei, G. Loi, B. Elsener, G. Rossi, A. Rossi, Arsenopyrite and pyrite bioleaching: evidence from XPS, XRD and ICP techniques, Anal. Bioanal. Chem. 401(7) (2011) 2237-2248.

[2] L.R. Reyes-Gutierrez, E.T. Romero-Guzman, A. Cabral-Prieto, R. Rodriguez-Castillo, Characterization of Chromium in Contaminated Soil Studied by SEM, EDS, XRD and Mossbauer Spectroscopy, J. Miner. Mater. Characterization Eng. 7(1) (2007) 59-70.

[3] M. Wang, E. Akiyama, K. Tsuzaki, Effect of hydrogen on the fracture behavior of high strength steel during slow strain rate test, Corros. Sci. 49(11) (2007) 4081-4097.

[4] F.G. Wei, T. Hara, K. Tsuzaki, Precise determination of the activation energy for desorption of hydrogen in two Ti-added steels by a single thermal-desorption spectrum, Metall. Mater. Trans. B 35(3) (2004) 587-597.

[5] S.-H. Yu, S.-M. Lee, S. Lee, J.-H. Nam, J.-S. Lee, C.-M. Bae, Y.-K. Lee, Effects of lamellar structure on tensile properties and resistance to hydrogen embrittlement of pearlitic steel, Acta Mater. 172 (2019) 92-101.

[6] J.A. Ronevich, B.C. De Cooman, J.G. Speer, E. De Moor, D.K. Matlock, Hydrogen Effects in Prestrained Transformation Induced Plasticity Steel, Metall. Mater. Trans. A 43(7) (2012) 2293-2301.

[7] D. Di Stefano, R. Nazarov, T. Hickel, J. Neugebauer, M. Mrovec, C. Elsässer, First-principles investigation of hydrogen interaction with TiC precipitates in α-Fe, Phys. Rev. B 93(18) (2016) 184108.

[8] M. Koyama, H. Springer, S.V. Merzlikin, K. Tsuzaki, E. Akiyama, D. Raabe, Hydrogen embrittlement associated with strain localization in a precipitation-hardened Fe–Mn–Al–C light weight austenitic steel, Int. J. Hydrogen Energy 39(9) (2014) 4634-4646.

[9] R. Silverstein, B. Glam, D. Eliezer, D. Moreno, S. Eliezer, Dynamic deformation of hydrogen charged austenitic-ferritic steels: Hydrogen trapping mechanisms, and simulations, J. Alloys Compd. 731 (2018) 1238-1246.

[10] A. Drexler, T. Depover, S. Leitner, K. Verbeken, W. Ecker, Microstructural based hydrogen diffusion and trapping models applied to Fe–C X alloys, J. Alloys Compd. 826 (2020) 154057.

[11] A. Nagao, M. Dadfarnia, B.P. Somerday, P. Sofronis, R.O. Ritchie, Hydrogen-enhanced-plasticity mediated decohesion for hydrogen-induced intergranular and “quasi-cleavage” fracture of lath martensitic steels, J. Mech. Phys. Solids 112 (2018) 403-430.

[12] J.P. Hirth, Effects of hydrogen on the properties of iron and steel, Metall. Trans. A 11(6) (1980) 861-890.

[13] M. Itakura, H. Kaburaki, M. Yamaguchi, T. Okita, The effect of hydrogen atoms on the screw dislocation mobility in bcc iron: A first-principles study, Acta Mater. 61(18) (2013) 6857-6867.
[14] J. Takahashi, K. Kawakami, Y. Kobayashi, Origin of hydrogen trapping site in vanadium carbide precipitation strengthening steel, Acta Mater. 153 (2018) 193-204.
[15] S. Echeverri Restrepo, D. Di Stefano, M. Mrovec, A.T. Paxton, Density functional theory calculations of iron - vanadium carbide interfaces and the effect of hydrogen, Int. J. Hydrogen Energy 45(3) (2020) 2382-2389.
[16] W. Krieger, S.V. Merzlikin, A. Bashir, A. Szczepaniak, H. Springer, M. Rohwerder, Spatially resolved localization and characterization of trapped hydrogen in zero to three dimensional defects inside ferritic steel, Acta Mater. 144 (2018) 235-244.
[17] K. Takai, Y. Homma, K. Izutsu, M. Nagumo, Identification of trapping sites in high-strength steels by secondary ion mass spectrometry for thermally desorbed hydrogen, J. Jpn. Inst. Metals 60(12) (1996) 1155-1162.
[18] F.G. Wei, K. Tsuzaki, Quantitative analysis on hydrogen trapping of TiC particles in steel, Metall. Mater. Trans. A 37(2) (2006) 331-353.
[19] I.M. Bernstein, The effect of hydrogen on the deformation of iron, Scr. Metall. 8(4) (1974) 343-349.
[20] T. Depover, K. Verbeken, The effect of TiC on the hydrogen induced ductility loss and trapping behavior of Fe-C-Ti alloys, Corros. Sci. 112 (2016) 308-326.
[21] W.Y. Choo, J.Y. Lee, Thermal analysis of trapped hydrogen in pure iron, Metall. Trans. A 13(1) (1982) 135-140.
[22] K. Kawakami, T. Matsumiya, Numerical analysis of hydrogen trap state by TiC and V_4C_3 in bcc-Fe, ISIJ Int. 52(9) (2012) 1693-1697.
[23] T. Depover, K. Verbeken, The detrimental effect of hydrogen at dislocations on the hydrogen embrittlement susceptibility of Fe-C-X alloys: An experimental proof of the HELP mechanism, Int. J. Hydrogen Energy 43(5) (2018) 3050-3061.

[24] E. Wallaert, T. Depover, M. Arafin, K. Verbeken, Thermal desorption spectroscopy evaluation of the hydrogen-trapping capacity of NbC and NbN precipitates, Metall. Mater. Trans. A 45(5) (2014) 2412-2420.
[25] E. Wallaert, T. Depover, M. Arafin, K. Verbeken, Thermal Desorption Spectroscopy Evaluation of the Hydrogen-Trapping Capacity of NbC and NbN Precipitates, Metall. Mater. Trans. A 45(5) (2014) 2412-2420.
[26] X. Jin, L. Xu, W. Yu, K. Yao, J. Shi, M. Wang, The effect of undissolved and temper-induced (Ti,Mo)C precipitates on hydrogen embrittlement of quenched and tempered Cr-Mo steel, Corros. Sci. 166 (2020) 108421.
[27] D. Guedes, L. Cupertino Malheiros, A. Oudriss, S. Cohendoz, J. Bouhattate, J. Creus, F. Thébault, M. Piette, X. Feaugas, The role of plasticity and hydrogen flux in the fracture of a tempered martensitic steel: A new design of mechanical test until fracture to separate the influence of mobile from deeply trapped hydrogen, Acta Mater. 186 (2020) 133-148.
[28] Y.H. Fan, B. Zhang, H.L. Yi, G.S. Hao, Y.Y. Sun, J.Q. Wang, E.H. Han, W. Ke, The role of reversed austenite in hydrogen embrittlement fracture of S41500 martensitic stainless steel, Acta Mater. 139 (2017) 188-195.
[29] H. Fu, W. Wang, X. Chen, G. Pia, J. Li, Fractal and multifractal analysis of fracture surfaces caused by hydrogen embrittlement in high-Mn twinning/transformation-induced plasticity steels, Appl. Surf. Sci. 470 (2019) 870-881.
[30] S.-I. Lee, J.-M. Lee, S.-Y. Lee, H.-J. Kim, J.-Y. Suh, J.-H. Shim, U.-B. Baek, S.-H. Nahm, J. Lee, B. Hwang, Tensile and fracture behaviors of austenitic high-manganese steels subject to different hydrogen embrittlement test methods, Mater. Sci. Eng. A 766 (2019) 138367.
[31] K.-S. Kim, J.-H. Kang, S.-J. Kim, Nitrogen effect on hydrogen diffusivity and hydrogen embrittlement behavior in austenitic stainless steels, Scr. Mater. 184 (2020) 70-73.
[32] L.R. Queiroga, G.F. Marcolino, M. Santos, G. Rodrigues, C. Eduardo dos Santos, P. Brito, Influence of machining parameters on surface roughness and

susceptibility to hydrogen embrittlement of austenitic stainless steels, Int. J. Hydrogen Energy 44(54) (2019) 29027-29033.
[33] Q. Liu, Q. Zhou, J. Venezuela, M. Zhang, A. Atrens, Hydrogen influence on some advanced high-strength steels, Corros. Sci. 125 (2017) 114-138.
[34] X.Z. Liang, G.H. Zhao, M.F. Dodge, T.L. Lee, H.B. Dong, P.E.J. Rivera-Díaz-del-Castillo, Hydrogen embrittlement in super duplex stainless steels, Materialia 9 (2020) 100524.
[35] G. Egels, R. Fussik, S. Weber, W. Theisen, On the role of nitrogen on hydrogen environment embrittlement of high-interstitial austenitic CrMnC(N) steels, Int. J. Hydrogen Energy 44(60) (2019) 32323-32331.
[36] M. Alnajjar, F. Christien, C. Bosch, K. Wolski, A comparative study of microstructure and hydrogen embrittlement of selective laser melted and wrought 17–4 PH stainless steel, Mater. Sci. Eng. A 785 (2020) 139363.
[37] E. Ohaeri, J. Omale, K.M.M. Rahman, J. Szpunar, Effect of post-processing annealing treatments on microstructure development and hydrogen embrittlement in API 5L X70 pipeline steel, Mater. Charact. 161 (2020) 110124.
[38] S. Li, M. Liu, Y. Ren, Y. Wang, Hydrogen embrittlement behaviors of additive manufactured maraging steel investigated by in situ high-energy X-ray diffraction, Mater. Sci. Eng. A 766 (2019) 138341.
[39] E. Agyenim-Boateng, S. Huang, J. Sheng, G. Yuan, Z. Wang, J. Zhou, A. Feng, Influence of laser peening on the hydrogen embrittlement resistance of 316L stainless steel, Surface and Coatings Technology 328 (2017) 44-53.
[40] X. Chen, L. Ma, C. Zhou, Y. Hong, H. Tao, J. Zheng, L. Zhang, Improved resistance to hydrogen environment embrittlement of warm-deformed 304 austenitic stainless steel in high-pressure hydrogen atmosphere, Corros. Sci. 148 (2019) 159-170.
[41] T. Zhang, W. Zhao, T. Li, Y. Zhao, Q. Deng, Y. Wang, W. Jiang, Comparison of hydrogen embrittlement susceptibility of three cathodic protected subsea pipeline steels from a point of view of hydrogen permeation, Corros. Sci. 131 (2018) 104-115.

[42] H.-S. Noh, J.-H. Kang, K.-M. Kim, S.-J. Kim, The effects of replacing Ni with Mn on hydrogen embrittlement in Cr-Ni-Mn-N austenitic steels, Corros. Sci. 152 (2019) 93-100.

[43] Y. Wang, X. Wu, X. Li, W. Wu, J. Gong, Combined effects of prior plastic deformation and sensitization on hydrogen embrittlement of 304 austenitic stainless steel, Int. J. Hydrogen Energy 44(13) (2019) 7014-7031.